



ARTICLE

Cell-wide mapping of Orai1 channel activity reveals functional heterogeneity in STIM1-Orai1 puncta

Joseph L. Dynes^{1*}, Andriy V. Yeromin^{1*} , and Michael D. Cahalan^{1,2} 

Upon Ca²⁺ store depletion, Orai1 channels cluster and open at endoplasmic reticulum–plasma membrane (ER–PM) junctions in signaling complexes called puncta. Little is known about whether and how Orai1 channel activity may vary between individual puncta. Previously, we developed and validated optical recording of Orai channel activity, using genetically encoded Ca²⁺ indicators fused to Orai1 or Orai3 N or C termini. We have now combined total internal reflection fluorescence microscopy with whole-cell recording to map functional properties of channels at individual puncta. After Ca²⁺ store depletion in HEK cells cotransfected with mCherry-STIM1 and Orai1-GCaMP6f, Orai1-GCaMP6f fluorescence increased progressively with increasingly negative test potentials and robust responses could be recorded from individual puncta. Cell-wide fluorescence half-rise and -fall times during steps to –100 mV test potential indicated probe response times of <50 ms. The in situ Orai1-GCaMP6f affinity for Ca²⁺ was 620 nM, assessed by monitoring fluorescence using buffered Ca²⁺ solutions in “unroofed” cells. Channel activity and temporal activation profile were tracked in individual puncta using image maps and automated puncta identification and recording. Simultaneous measurement of mCherry-STIM1 fluorescence uncovered an unexpected gradient in STIM1/Orai1 ratio that extends across the cell surface. Orai1-GCaMP6f channel activity was found to vary across the cell, with inactive channels occurring in the corners of cells where the STIM1/Orai1 ratio was lowest; low-activity channels typically at edges displayed a slow activation phase lasting hundreds of milliseconds. Puncta with high STIM1/Orai1 ratios exhibited a range of channel activity that appeared unrelated to the stoichiometric requirements for gating. These findings demonstrate functional heterogeneity of Orai1 channel activity between individual puncta and establish a new experimental platform that facilitates systematic comparisons between puncta composition and activity.

Introduction

In many cell types, Orai proteins in the plasma membrane (PM) form Ca²⁺ channels that are activated by STIM proteins in the ER to mediate store-operated Ca²⁺ entry (SOCE; Cahalan, 2009). The resulting Ca²⁺ influx, earlier named Ca²⁺ release-activated Ca²⁺ (CRAC) current (Hoth and Penner, 1992), is characterized biophysically by extremely low single-channel conductance, a high degree of selectivity for Ca²⁺ ions in physiological saline, permeability to small monovalent cations when external Ca²⁺ is reduced, block by trivalent cations, and Ca²⁺-induced inactivation (Hoth and Penner, 1993; Lepple-Wienhues and Cahalan, 1996; Lewis and Cahalan, 1989; Zweifach and Lewis, 1995), as reviewed (Amcheslavsky et al., 2015; Prakriya and Lewis, 2015). At the cellular level, functional roles of Orai1 have now been established in lymphocytes, natural killer cells, mast cells, platelets, sweat and salivary glands, dentition, vascular smooth muscle, endothelial cells, skeletal muscle, microglia, astrocytes, and developing and adult neurons (Feske, 2009; Gao et al., 2016;

Kraft, 2015; Kwon et al., 2017; Lewis, 2011; Papanikolaou et al., 2017; Sharma and Ping, 2014; Toth et al., 2016; Tshuva et al., 2017). Loss-of-function point mutations in either STIM1 or Orai1 cause severe combined immune disorder (Byun et al., 2010; Feske et al., 2006; McCarl et al., 2009, 2010; Picard et al., 2009), whereas gain-of-function mutations in either gene cause Stormorken syndrome characterized by low platelet count and muscle weakness (Böhm and Laporte, 2018; Misceo et al., 2014; Morin et al., 2014; Nesin et al., 2014), as reviewed (Feske, 2019; Lacruz and Feske, 2015).

Upon ER Ca²⁺ store depletion, STIM1 proteins in the ER and Orai1 channels in the PM cluster together at ER–PM junctions, where the hexameric Orai1 channels are opened by coordinated binding of STIM1 dimers (Amcheslavsky et al., 2015; Prakriya and Lewis, 2015). These STIM1–Orai1 puncta, constituting the elementary unit of SOCE (Luik et al., 2006), are small (100–300 nm in diameter; Chang et al., 2017), discrete, and relatively

¹Department of Physiology and Biophysics, University of California at Irvine School of Medicine, Irvine, CA; ²Institute for Immunology, University of California, Irvine, Irvine, CA.

*J.L. Dynes and A.V. Yeromin contributed equally to this paper; Correspondence to Michael D. Cahalan: mcahalan@uci.edu; Joseph L. Dynes: jdynes@uci.edu.

© 2020 Dynes et al. This article is distributed under the terms of an Attribution–Noncommercial–Share Alike–No Mirror Sites license for the first six months after the publication date (see <http://www.rupress.org/terms/>). After six months it is available under a Creative Commons License (Attribution–Noncommercial–Share Alike 4.0 International license, as described at <https://creativecommons.org/licenses/by-nc-sa/4.0/>).

evenly spaced around the cell (Hsieh et al., 2017). In over-expression systems, individual puncta are packed with Orail channels, containing 100–1,000 Orail channels that are, on average, 15 nm apart in a dense but irregular array (Perni et al., 2015). The molecular choreography of STIM1-Orail interaction leads to several possibilities for the stoichiometry of channel gating, including varying numbers of STIM1 dimers that interact with adjacent Orail subunits in a single hexameric Orail channel (Yen and Lewis, 2018, 2019) or cross-link two adjacent Orail channels (Zhou et al., 2015). Previous studies have reported changes in both the magnitude and properties of Orail currents, depending on the ratio of STIM1:Orail (McNally et al., 2012; Yen and Lewis, 2018, 2019).

Despite the importance of Orail in cell physiology and as a potential therapeutic target, mechanistic questions about gating, local signaling at puncta, and downstream actions of Ca^{2+} remain at single channel, puncta, and cellular levels. These questions could be addressed, in part, by the ability to visualize Orail channel activity within cells. For this approach, we developed fusions of both Orail and Orail3 channels with a variety of C- or N-terminally tethered fluorescent genetically encoded Ca^{2+} indicators (GECI; Dynes et al., 2016). These channel-indicator constructs report activation of Orail upon ER store depletion, revealing the sites of SOCE with high dynamic range. They are functional following transfection into different cell types, including widely used human embryonic kidney (HEK) 293A cells and human T cells. Moreover, these fusions are sufficiently bright to detect the activity of individual Orail channels using TIRF microscopy, in part because each hexameric Orail channel has six Ca^{2+} indicators that can potentially respond to Ca^{2+} influx when the channel opens.

Our optical recording approach allows us to image Orail channel activity across the cell and in several cells simultaneously, enabling precise localization and potentially leading toward opportunities to uncover basic mechanisms of Orail gating and sub-cellular organization. Here, we characterize the performance of an Orail-GCaMP6f fusion in HEK 293A cells, using simultaneous whole-cell recording and TIRF imaging (Patch-TIRF). Patch-TIRF enables precise control of Ca^{2+} entry for measuring kinetic responses of the Orail-GCaMP6f fluorescence reporter and for associating Orail-GCaMP6f current and fluorescence. Unroofing of cells exposes Orail-GCaMP6f proteins to the extracellular environment in situ where their Ca^{2+} binding affinity could be determined. Moreover, TIRF imaging of Orail-GCaMP6f allows us to map Orail channel activity within individual cells. These experiments reveal heterogeneity in Orail channel activity between puncta within the same cell, which was caused in part by local differences in the ratio of STIM1:Orail at puncta.

Materials and methods

Cells and transfections

HEK 293A cells (Thermo Fisher Scientific) were incubated at 37°C, 5% (vol/vol) CO_2 , and maintained in Dulbecco's modified Eagle's medium (DMEM; Lonza) supplemented with 10% FBS (Omega Scientific) and 2 mM L-glutamine (Sigma-Aldrich). Cells

were transfected in six-well plates at 90% confluence using Lipofectamine 3000 (Thermo Fisher Scientific) according to the manufacturer's instructions. DNA constructs encoding fusion of the red fluorescent protein mCherry to the processed N terminus of human STIM1, mCherry-STIM1 (Ellefsen et al., 2015; Perni et al., 2015), and the genetically encoded Ca^{2+} indicator GCaMP6f to the C terminus of human Orail, Orail-GCaMP6f (Dynes et al., 2016) were used to transfect HEK 293A cells. For Patch-TIRF experiments, a total of 2.5 μg of DNA at a 2:1 ratio of mCherry-STIM1 to Orail-GCaMP6f was used for transfection. 1 d after transfection, cells were dissociated from the culture surface with TrypLE Express (Thermo Fisher Scientific), spun down, resuspended in DMEM + 10% FBS + glutamine, and plated onto poly-L-lysine-coated coverslips (>300,000 MW, 0.1 mg/ml in water; Sigma-Aldrich) overnight. To assess Orail-GCaMP6f biophysical properties, 500 ng of mCherry-STIM1 and 50 ng of Orail-GCaMP6f were cotransfected into HEK 293A cells. 12–24 h later, transfected cells were dissociated from the culture surface with TrypLE and replated 1–4 h before whole-cell recording.

Whole-cell recording

Patch clamp experiments were performed at room temperature. Data were acquired using an EPC9 patch clamp amplifier (HEKA) at 5 kHz sampling rate and digitally filtered at 1–2 kHz for analysis and display. The pipette resistance was 2–5 M Ω when filled with internal solutions; pipette capacitance was completely compensated and series resistance was 80% compensated by EPC-9 circuitry; seal resistance was >10 G Ω . Membrane potentials were corrected for a liquid junction potential between the pipette and bath solutions depending on internal solution composition (see Solutions). To assess Orail-GCaMP6f biophysical properties in the absence of simultaneous TIRF imaging, the membrane potential was held at 0 mV, and voltage ramps from –120 to +100 mV alternating with 220-ms pulses to –120 mV were applied every 2 s. All I–V curves are averages of five traces and leak subtracted. Leak was recorded after 10 μM GdCl_3 was applied to block Orail current and fitted with a fifth order polynomial function. During simultaneous imaging and patch clamp experiments, longer pulses up to 600 ms in duration were applied episodically, and voltage ramps were not applied. Solutions with different ion composition were applied through a gravity-driven local perfusion system, and complete local solution exchange was achieved within ~2 s. Data were analyzed using Pulse (Heka Electronic), Microsoft Excel (Microsoft), and Origin (OriginLab Corp.).

Solutions

The composition of external solutions is listed in Table 1. For simultaneous imaging and whole-cell recording, the pipette solution contained (in mM) 122 CsAsp, 12 Cs_4EGTA , 2 CsCl, 10 MgGluconate_2 , 2 Na_2ATP , 15 HEPES, 20 μM inositol 1,4,5 triphosphate (IP_3), pH 7.2, osmolality 301 mOsm (liquid junction potential 13 mV). For studies of biophysical properties of Orail-GCaMP6f, the pipette solution contained (in mM) 131 CsAsp, 10 Cs_4BAPTA , 2 CsCl, 8 MgGluconate_2 , 15 HEPES, 2 μM IP_3 , pH 7.2, osmolality 320 mOsm (liquid junction potential 11 mV).

Table 1. External solutions

External solutions used in combined TIRF/patch clamp experiments				
Name	NaCl	CholineCl	CaCl ₂	Sucrose
Ca2	151.5	—	2	8
Ca0	151.5	4	—	8
Ca0.2	151.5	3.6	0.2	8
Ca0.6	151.5	2.8	0.6	8
Ca20	115.5	—	20	28
External solutions used in patch clamp only experiments				
Name	NaCl		CaCl ₂	
Ca2	152		2	
Ca20	129		20	
Na DVF	160		—	

Ca0 solution contained 2 mM EGTA. All solutions in top half contained (in mM) 4.5 KCl, 1 MgCl₂, 10 glucose, and 15 HEPES; pH was adjusted to 7.4 with NaOH; osmolality 325 mOsm. All solutions in bottom half contained (in mM) 10 glucose and 10 HEPES; pH was adjusted to 7.4 with NaOH. Ca2 and Ca20 solutions contained 4.5 mM KCl and 1 mM MgCl₂. Na DVF solution contained 2 mM *N*-(2-Hydroxyethyl)ethylenediamine-*N,N',N'*-triacetic acid (HEDTA). Osmolality of all external solutions was 325 mOs.

TIRF microscopy

TIRF imaging was performed on an Olympus IX81 microscope with a home-built TIRF illumination system, as described (Dynes et al., 2016). TIRF illumination lasers were introduced into the optical path by way of a micrometer-positioned 5-mm mirror-coated prism placed near the back focal plane of the objective. The imaging system consisted of an Olympus 60× 1.45 NA PlanApoN TIRF objective, Photometrics DualView2 image splitter with Chroma T565lpxr dichroic mirror and Semrock 520/28 and 624/40 emission filters, Photometrics Evolve 512 electron multiplying charge-coupled device (EMCCD) camera, a 488-nm argon ion laser (Ion Laser Technology) and 561-nm solid-state Diode-pumped solid-state (DPSS) laser (Lasos), and a Prior Proscan motorized stage. Using the 60× TIRF objective, a pixel corresponds to a 267-nm square. The system was controlled with Metamorph 7 software (Molecular Devices). Two-color images, monitoring Orai1-GCaMP6f activity in green and mCherry-STIM1 in red, were acquired simultaneously using the DualView from samples illuminated simultaneously using both lasers. Illumination intensities for simultaneous imaging and patch clamp experiments were ~30 and ~4 W/cm² for the 488-nm and 561-nm lasers, respectively, and ~1 W/cm² for imaging unroofed cells. Image streams were acquired episodically at 50 frames/s using regions of interest (ROIs) with heights of <256 pixels (half the EMCCD size). 16-bit images were acquired using an EM camera gain of 130. Image streams were synchronized with whole-cell recordings using transistor-transistor logic pulses sent via an analogue-to-digital converter computer card (IOtech) driven by Metamorph during image acquisition. Simultaneous imaging and patch clamp experiments were performed at ~25°C.

Protocols for combined Patch-TIRF experiments

A series of electrophysiological and solution exchange protocols was delivered to each cell in the same order. Cell holding

potential was +20 mV. Initially, a series of repeated 600-ms test pulses to -100 mV were given as cells were exposed to an ascending series of extracellular Ca²⁺ concentrations (0.2, 0.6, 2, and 20 mM nominal). Subsequently, a series of increasingly negative test potentials (-10, -40, -70, and -100 mV) was delivered to cells in 2 mM extracellular Ca²⁺. Cells were then unroofed for probe calibration or subjected to an additional series of consecutive 300-ms steps to increasingly negative test potentials (-10, -40, and -70 mV), followed by a final 600 ms step to -100 mV, and then unroofed. Cells were perfused in 0.2 mM extracellular Ca²⁺ in between protocols to minimize Ca²⁺-dependent inactivation of Orai1-GCaMP6f currents, and the external perfusion solution was switched 5 s before test pulse delivery. Typically, the interval between test pulses was 20–60 s.

Image processing and fluorescence measurements

Image processing and measurement were performed with the freely available image processing program ImageJ version 1.50 produced by the Research Services Branch of the National Institutes of Mental Health and Neurological Disorders and Stroke (Schneider et al., 2012). TIRF images were background-subtracted using the mean value of a manually selected ROI near the cell of interest. Baseline images were produced by averaging 10 consecutive frames acquired at 50 Hz for 200 ms before the start of the 600-ms test pulse; rising phase images were produced by averaging 10 frames at 50 Hz from the first third of the test pulse, and plateau-phase images were similarly produced from the last third of the test pulse. Masks for ΔF/F₀ and Activation index (A-index) images were produced from plateau-phase images using the “Auto Local Threshold” function of ImageJ by choosing the “Niblack” segmentation method and setting the radius to 5 pixels; regions outside the footprint were excluded manually. ΔF/F₀ maps were produced by dividing the plateau-phase image by the baseline image and masking the

result. A-index maps were produced by dividing a baseline-subtracted rising phase image by a baseline-subtracted plateau-phase image and masking the result. For recording Orai1-GCaMP6f fluorescence, puncta were identified in modified plateau-phase images (average of 20 consecutive frames at 50 Hz 200–600 ms during the test pulse) using the “Find Maxima” function of ImageJ and setting the noise tolerance to 100–200. Single-pixel output maps were dilated by one pixel to generate 3×3 pixel ROI at every punctum; the resulting composite ROI including all puncta was used to record Orai1-GCaMP6f fluorescence traces. Kinetic measurements were performed using single pixel ROIs at every punctum. ROIs for selected single puncta traces were segmented manually from the composite ROIs.

Resting fluorescence (also known as baseline fluorescence or F_0) was calculated by averaging 10 consecutive measurements acquired at 50 Hz for 200 ms before the start of a test pulse (–200 to 0 ms); rising-phase fluorescence was calculated by averaging 10 consecutive measurements at 50 Hz from the first third of a 600-ms test pulse (0–200 ms), and plateau-phase fluorescence (also known as plateau fluorescence) was calculated by averaging 10 consecutive measurements at 50 Hz from the last third of a 600 ms test pulse (400–600 ms). For test pulses consisting of steps to increasingly negative membrane potentials, plateau fluorescence was calculated for each step by averaging five consecutive measurements at 50 Hz from the last third of each 300-ms step.

Cell unroofing and measurement of Orai1-GCaMP6f Ca^{2+} K_d

After whole-cell recording of an HEK 293A cell cotransfected with Orai1-GCaMP6f and mCherry-STIM1, the recording pipette was withdrawn and the tip was broken on the coverslip, forming a sharp edge. The cell was unroofed by carefully puncturing and scraping the broken pipette across the top surface of the cell under transmitted light illumination. Standard buffered Ca^{2+} solutions (Calcium Calibration Buffer Kit #1; Thermo Fisher Scientific) with K^+ as the primary cation and varying free Ca^{2+} concentrations were used in probe calibration runs. The kit consisted of two solutions containing 10 mM K_2EGTA (solution 1) and 10 mM $CaEGTA$ (solution 2), and 100 mM KCl and 30 mM $MOPS$, pH 7.2 (both solutions). Mixing of these solutions at different ratios generated standard Ca^{2+} buffers ranging from 0 to 39 μM free Ca^{2+} . These standard solutions were applied in series to the unroofed cell through a gravity-driven local perfusion system while two-channel fluorescence images were acquired. Unroofed cells were equilibrated in the perfusion stream for 20–30 s before image acquisition. At each Ca^{2+} concentration, green channel measurements were produced by subtracting the 0 nM Ca^{2+} measurement. Cell footprint ROIs were traced manually, and mean fluorescence values were measured. Fluorescence values were plotted, and K_d and Hill coefficients (hc) were calculated using Prism 8 (GraphPad Software).

Modeling the response function of Orai1-GCaMP6f

Plateau fluorescence (F) and I measurements during steps to increasingly negative membrane potential (–10, –40, –70, and –100 mV in 2 Ca) were graphed as a scatter plot and fitted to the Hill equation using nonlinear regression, as well as fitted using

linear regression, both calculated using GraphPad Prism 8. To analyze responses to individual test pulses in six cells, whole-cell current and fluorescence were normalized using the current from cell A at –40 mV as a reference. Normalized whole-cell current and fluorescence from stepped test pulses were fitted as a scatter plot independently from responses to individual test pulses when comparing fitted Hill equations.

Measurement of Orai1-GCaMP6f kinetics

Non-linear curve fits, residual analysis, and rise and fall times were calculated and plotted using Prism 8 (GraphPad Software). Traces were normalized using the plateau-phase value from each cell. After fitting the Orai1-GCaMP6f fluorescence rising phase to a single exponential curve, residual analysis revealed systematic deviation of the fluorescence intensity values from the least-squares minimized curve fit. Since a two-phase exponential association curve did not converge upon a solution, the Orai1-GCaMP6f fluorescence rise was fitted to the sum of single-exponential and linear functions. Because Orai1-GCaMP6f fluorescence reached a peak in the first 100–150 ms after stepping to –100 mV in 20 mM Ca^{2+} , and because of the quality of the fit, the rise in Orai1-GCaMP6f fluorescence in 20 mM Ca^{2+} was fitted to the first 150 ms of the response.

Automated puncta identification and recording, and measurement of relative STIM1/Orai1 ratio

The Fiji/ImageJ plugin TrackMate version 4.0.0 (Tinevez et al., 2017) was used to automatically identify and record Orai1-GCaMP6f and mCherry-STIM1 fluorescence from puncta. To facilitate tracking of dim puncta, a low-noise offset, corresponding to the average of 10 baseline images acquired 200–0 ms before a test pulse, was added to each frame in a background-subtracted image stack. The low-noise offset image was appended to the end of each stack as well, so the value of the fluorescence offset could be measured at each punctum and subsequently subtracted from each puncta trace. mCherry-STIM1 and Orai1-GCaMP6f image stacks obtained during hyperpolarizing test pulses were manually aligned and concatenated, so each punctum would be associated with a corresponding mCherry-STIM1 and Orai1-GCaMP6f response. TrackMate settings included use of the log of Gaussian detector for identifying particles, estimated “blob” diameter of 3.0 pixels (800 nm), threshold of 200, use of the simple Linear Assignment Problem tracking algorithm (Jaqaman et al., 2008), linking distance of 2.0 pixels (530 nm), and selection of only those puncta traces that included every frame. Fluorescence from manually unroofed cells in 0 mM and 2 mM Ca^{2+} was associated with a given puncta fluorescence response by appending the unroofed cell images to the end of the respective image stacks; in this case, the low noise offset was not added to enable lateral tracking of puncta that might have been displaced by cell unroofing. Calculations were performed using Excel version 16.30 (Microsoft), and puncta responses were plotted using Prism 8 (GraphPad Software). Values of puncta fluorescence measured in arbitrary units were almost identical to values measured in photons, as puncta ROIs contained 21 pixels, while at each pixel, 1 photon equals 21.7 arbitrary units.

Relative STIM1/Orai1 ratio at each punctum was calculated by dividing the mean resting, background-subtracted fluorescence for mCherry-STIM1 by the corresponding Orai1-GCaMP6f fluorescence value; fluorescence means were calculated from 10 baseline images acquired 200–0 ms before a test pulse. Relative STIM1/Orai1 ratio measurements were standardized to the responses from our third acquisition protocol, 600 ms test pulse to -100 mV in 2 mM external Ca^{2+} . Puncta STIM1/Orai1 ratio, fractional activation, and Ca^{2+} current bubble plots were created in Mathematica version 12.0.0 (Wolfram Research). Linear curve fitting of Orai1-GCaMP6f $\Delta F/F_0$ v. STIM1/Orai1 ratio was performed using Prism 8 (GraphPad Software).

The positions of puncta detected by TrackMate were compared with the positions of puncta in super-resolution radial fluctuations (SRRF; Gustafsson et al., 2016) images of mCherry-STIM1. 50 consecutive mCherry-STIM1 frames, starting 10 frames before the delivery of a test pulse, were processed using the SRRF ImageJ plugin (version 1.1 Stable0) at the default settings: ring radius of 0.5, radially magnification of 4, and the number of axes in ring of 6.

Orai1-GCaMP6f measurement variability and relative STIM1/Orai1 ratio stability

The variability in Orai1-GCaMP6f $\Delta F/F_0$ measurements within a trace was calculated for each punctum using pairs of fluorescence intensity values occurring 1.2 and 1.8 s after cessation of the test pulse; each value corresponded to the average of 10 consecutive Orai1-GCaMP6f fluorescence measurements. The fractional difference between the two measurements was calculated for each punctum, and the SD of the entire population was calculated using Prism 8. The signal-to-noise ratio was expressed as the reciprocal of the SD.

To measure the stability of resting Orai1-GCaMP6f fluorescence and relative STIM1/Orai1 ratio, resting fluorescence from cells A–F was measured in whole footprints using manually selected ROIs and individual puncta automatically identified using TrackMate. To detect fluctuations in local $[\text{Ca}^{2+}]$, Orai1-GCaMP6f resting fluorescence was normalized to the average value before the four test pulses. Fluctuations in relative STIM1/Orai1 ratio for each punctum from each cell were calculated from resting Orai1-GCaMP6f and mCherry-STIM1 values and normalized to the average value before the four test pulses.

Calculation of single puncta $[\text{Ca}^{2+}]$ and current

Single puncta currents were derived by apportioning whole-cell current at the plateau of a response to a 600-ms test pulse to -100 mV. Three linked equations, expressed as ratios, were used to calculate single puncta currents. First, area of the TIRF footprint was used to calculate the current through only those Orai1-GCaMP6f channels present in the TIRF footprint. Whole-cell surface area (CellA) was determined from cell capacitance using the conversion of 1 pF per $100 \mu\text{m}^2$ (Neher and Marty, 1982). Footprint area (FPA) was calculated using the size of a pixel ($0.071 \mu\text{m}^2$) and the number of pixels in the footprint, defined by a manually selected ROI. Current through channels in the footprint ($\text{FPI}_{\text{plateau}}$) equaled the plateau whole-cell current ($\text{CellI}_{\text{plateau}}$) times FPA divided by CellA . Similar scaling by area when calculating the Orai1-GCaMP6f response function yielded

an excellent fit to the Hill equation, indicating that channel activity within the TIRF footprint was representative of the cell surface as a whole. Second, Orai1-GCaMP6f fluorescence was used to calculate the current through the subset of puncta that was automatically identified (i.e., tracked). This step was necessary because not all puncta in the footprint were identified by the particle tracking program. Mean plateau fluorescence of the footprint was measured from TIRF images and multiplied by the number of pixels in the footprint to calculate the footprint fluorescence ($\text{FPF}_{\text{plateau}}$). For automatically identified puncta, the sum of plateau fluorescence from all puncta was calculated using Microsoft Excel and multiplied by the number of pixels in the fixed-size ROI used for automated recording of puncta (21) to calculate the fluorescence from automatically identified puncta ($\text{PTrackF}_{\text{plateau}}$). Current through tracked puncta ($\text{PTrackI}_{\text{plateau}}$) equaled $\text{FPF}_{\text{plateau}}$ times $\text{PTrackF}_{\text{plateau}}$ divided by $\text{FPF}_{\text{plateau}}$. Third, puncta $[\text{Ca}^{2+}]$ and resting Orai1-GCaMP6f fluorescence were used to calculate the current through single puncta. Nominal $[\text{Ca}^{2+}]$ at each punctum was calculated using the Hill equation from the fractional saturation of Orai1-GCaMP6f, determined using zero and saturated Ca^{2+} puncta fluorescence from unroofed cells, and our experimentally determined values of K_d and h_c . For a given punctum (P1), the product of $\text{P1}[\text{Ca}^{2+}]_{\text{plateau}}$ and resting Orai1-GCaMP6f fluorescence (P1F_{rest}) was divided by $[\text{Ca}^{2+}]_{\text{plateau}}$ multiplied by F_{rest} summed over all automatically identified puncta. For each punctum, this ratio times $\text{PTrackI}_{\text{plateau}}$ equaled the single puncta current ($\text{P1I}_{\text{plateau}}$).

Statistical analysis and experimental replication

Data range, central tendency, and 95% confidence interval (CI) were calculated using Prism 8 (GraphPad Software). Values were plotted as mean \pm SEM. The individual traces shown are representative of traces from other cells. Replicate experiments were performed on multiple days.

Data and materials availability

All data needed to evaluate the conclusions in the paper are present in the paper or the online supplementary materials. Orai1-GCaMP6f and additional tandem GECI-Orai1 constructs are available from Addgene (<https://www.addgene.org/>).

Online supplemental material

Fig. S1 plots whole-cell current versus fluorescence with fitting to the Hill equation and linear regression. Fig. S2 illustrates automated puncta identification and recording. Fig. S3 plots resting fluorescence of mCherry-STIM1 and Orai1-GCaMP6f and resulting relative STIM1/Orai1 ratio for every punctum by cell (A–F). Fig. S4 illustrates the stability over time of Orai1-GCaMP6f resting fluorescence and relative STIM1/Orai1 ratio. Fig. S5 illustrates the calculation of single puncta currents.

Results

Simultaneous whole-cell recording and TIRF imaging of Orai1-GCaMP6f-expressing cells

We previously established that fusions of Orai1 and fluorescent GECIs detect Ca^{2+} influx in HEK 293A cells transiently

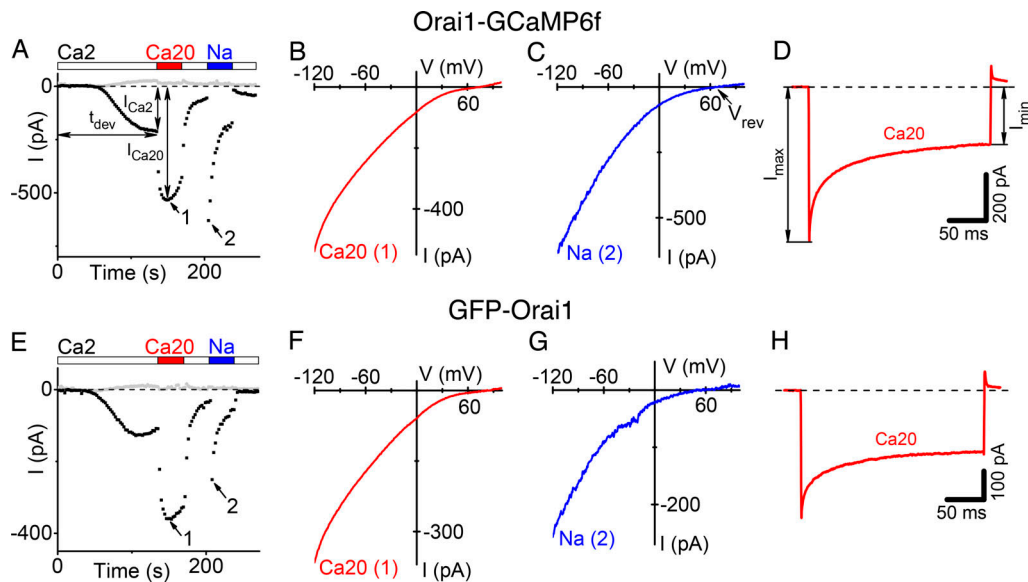


Figure 1. Biophysical properties of Orai1-GCaMP6f and GFP-Orai1 STIM1-operated currents. Representative whole-cell recordings from HEK 293A cells transiently cotransfected at a ratio of 10:1 with mCherry-STIM1 plus either Orai1-GCaMP6f (A–D, top; $n = 6$ cells) or GFP-Orai1 (E–H, bottom; $n = 6$ cells). **(A and E)** Leak-subtracted time course, following break-in to achieve whole-cell recording at time = 0, of Orai1-GCaMP6f (A) and GFP-Orai1 (E) STIM1-operated current recorded in response to ramp stimuli from -120 mV (black points) to $+100$ mV (gray points). **(B, C, F, and G)** Current-voltage relationship of Orai1-GCaMP6f (B and C) and GFP-Orai1 (F and G) current recorded in 20 mM Ca^{2+} (B and F) and Na^+ DVF (C and G) solutions, respectively. **(D and H)** Ca^{2+} -dependent inactivation of Orai1-GCaMP6f (D) and GFP-Orai1 (H) current during -120 mV hyperpolarizing pulse from a holding potential of 0 mV, recorded in 20 mM Ca^{2+} external solution. Bars indicate exchange of external solutions (see Table 1 for solution recipes). Arrows in A and D indicate the time points for I–V curves in B, C, F, and G. Lines with arrowheads indicate biophysical parameters presented in Table 2.

cotransfected with mCherry-STIM1 after depletion of ER Ca^{2+} stores (Dynes et al., 2016). Here, we sought to determine the response characteristics of Orai1-GECI fusions so we might translate their fluorescence signals into recordings of channel activity. Our approach made use of simultaneous whole-cell recording and TIRF imaging. Once Orai1-GECI channels were activated during Patch-TIRF, changing membrane potential allowed us to control Ca^{2+} influx through the channels, image Orai1-GECI responses, and, as a result, determine the relationship between channel current and fluorescence. We previously used patch clamp analysis to show that the N-terminal fusion G-GECO1-Orai1 is fully functional as a CRAC channel (Dynes et al., 2016), and here we used the C-terminal fusion Orai1-GCaMP6f for further analysis because of its high brightness and dynamic range, rapid rise and fall kinetics, and compatibility with multiple Orai1 translational start sites (Chen et al., 2013; Fukushima et al., 2012).

Fig. 1, A–D, illustrates biophysical properties of Orai1-GCaMP6f currents in HEK 293A cells transiently cotransfected with mCherry-STIM1 after depletion of ER Ca^{2+} stores by pipette dialysis with IP_3 . Inward currents developed with the expected kinetics (current development time, t_{dev} , in Fig. 1 A) and amplitudes in 2 mM external $[\text{Ca}^{2+}]$ ($I_{\text{Ca}2}$ in Fig. 1 A), and current amplitude increased twofold when external $[\text{Ca}^{2+}]$ was raised to 20 mM ($I_{\text{Ca}20}$ in Fig. 1 A). Replacement of the external solution with divalent-free (DVF) Na^+ solution resulted in a large inward current carried by Na^+ with the expected slow decline from peak values (Fig. 1 A). The I–V curves of currents recorded in 20 mM $[\text{Ca}^{2+}]$ (Fig. 1 B) and in DVF (Fig. 1 C) exhibited characteristics of

classic CRAC current, possessing a positive reversal potential (V_{rev}) in DVF indicative of high Na^+ permeability relative to Cs^+ (Fig. 1 C). Responses to test pulses to -120 mV showed the expected degree of fast inactivation (calculated by dividing the current at 200 ms, I_{min} , by the peak current, I_{max} ; Fig. 1 D). These properties were similar in control cells cotransfected with mCherry-STIM1 plus GFP-Orai1 (Fig. 1, E–H). A comparison of key biophysical parameters is shown in Table 2. By these measures, Orai1-GCaMP6f is fully functional as a CRAC channel.

HEK 293A cells were transiently cotransfected with Orai1-GCaMP6f and mCherry-STIM1 for simultaneous whole-cell recording and TIRF imaging (Fig. 2). Two-color TIRF was used to simultaneously image Orai1-GCaMP6f channels in the PM (Fig. 2, A–E) and mCherry-STIM1 in PM-adjacent portions of the ER (Fig. 2, F–J) during whole-cell recording and, in the same cell, after mechanical unroofing (see below). Two-day transfected cells selected for recording exhibited a very dim but uniform distribution of Orai1-GCaMP6f fluorescence in the PM (Fig. 2 A) and a moderate level of mCherry-STIM1 in the ER at rest (Fig. 2 F). After break-in to achieve whole-cell recording, ER stores were depleted by IP_3 diffusing into the cytosol from the patch pipette, and Orai1-GCaMP6f and mCherry-STIM1 clustered into puncta (Fig. 2, B and G). mCherry-STIM1 became brighter as it approached the PM and descended into the TIRF field. Crosstalk between neighboring puncta and Ca^{2+} -dependent run-down of Orai1-GCaMP6f responses were minimized by inclusion of 12 mM EGTA in the patch pipette, holding the membrane potential at $+20$ mV, and switching to external solutions containing 0.2 mM Ca^{2+} between protocols.

Table 2. Comparison of biophysical properties of GFP-Orai1 and Orai1-GCaMP6f STIM1-operated currents

Construct	t_{dev} s	I_{Ca2} density, pA/pF	I_{Ca20} density, pA/pF	I_{Ca20}/I_{Ca2}	V_{revDVF} , mV	I_{min}/I_{max}
GFP-Orai1 (6)	193 ± 54 ^a	8.1 ± 1.1	18.8 ± 2.3	2.37 ± 0.19	66 ± 3	0.39 ± 0.02
Orai1-GCaMP6f (6)	294 ± 88	13.1 ± 2.8	24.4 ± 5.0	1.94 ± 0.14	74 ± 4	0.36 ± 0.02
P value	0.36	0.14	0.34	0.09	0.14	0.30

Biophysical meaning of parameters is presented in Fig. 1. Data presented as mean ± SEM; number of cells used for calculations is indicated in parentheses. ^aTo calculate this value, $n = 5$.

Orai1-GCaMP6f fluorescence was stable at a low level at +20 mV holding potential and rapidly became brighter upon stepping to -100 mV in 2 mM external Ca^{2+} (Fig. 2 C). The magnitude of these cell-wide fluorescence responses ($\Delta F/F_0$) was between 0.7 and 2. During concurrent whole-cell recording and TIRF imaging, Orai1-GCaMP6f exhibited currents typical for cells co-transfected with DNA constructs encoding STIM1 and Orai1 at a 2:1 ratio and similar to currents recorded without simultaneous TIRF imaging in Fig. 1. Under these conditions, inward Ca^{2+} currents tended to increase slightly during the 600-ms test pulse (Fig. 2 K), consistent with a slow phase of activation observed for native CRAC currents in Jurkat cells (Christian et al., 1996; Zweifach and Lewis, 1996). mCherry-STIM1 exhibited no apparent change in intensity or localization during the test pulse (Fig. 2, G, H, and M). Resting Orai1-GCaMP6f fluorescence levels rapidly returned upon return to +20 mV holding potential (Fig. 2 L). In this way, a series of electrophysiological protocols could be delivered, and the resulting fluorescence changes recorded in the same cell without substantial run-down or photobleaching. Test pulses to -40 mV elicited Orai1-GCaMP6f

fluorescence responses that were lower in amplitude than those to -100 mV, and after a brief rising phase that may represent probe Ca^{2+} binding and activation kinetics, Orai1-GCaMP6f fluorescence and current exhibited parallel responses (Fig. 2, K and L). We note that fluorescence responses from similar GECI-Orai1 fusions were blocked by La^{3+} (Dynes et al., 2016). These results provide a proof-of-principle for simultaneous whole-cell recording and TIRF imaging of Orai1-GCaMP6f and STIM1 cotransfected cells and suggest proportionality between current and fluorescence responses.

Measurement of Orai1-GCaMP6f Ca^{2+} K_d and kinetics

To more precisely record Orai1 channel activity optically, we sought to determine the Ca^{2+} affinity and response kinetics of Orai1-tethered GECIs. After whole-cell recording, the recording pipette was removed from the cell and scraped across the top surface of the cell, opening the cytosol and basal PM to the extracellular environment. When performed carefully, this preparation leaves the basal PM intact (Fig. 2, D, E, I, and J) and allows for direct access to the cytoplasmic side of the basal PM.

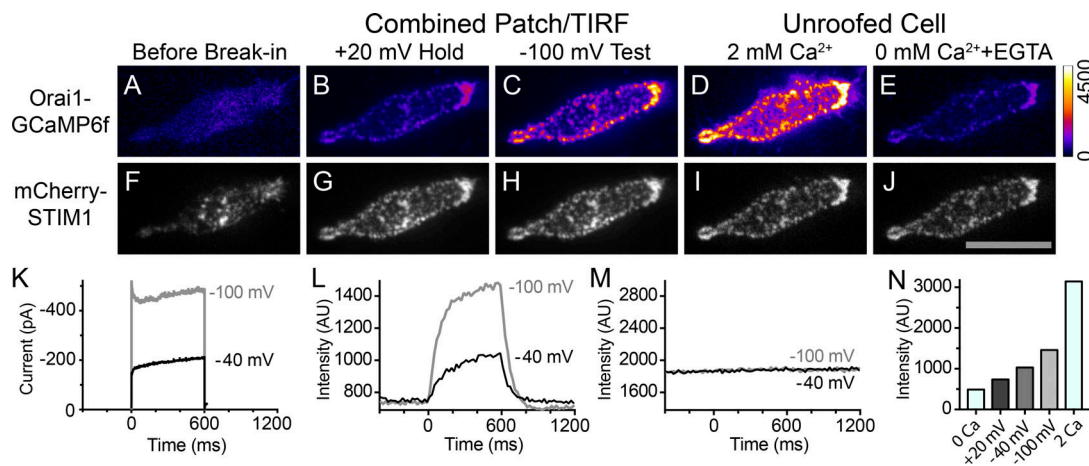


Figure 2. Orai1-GCaMP6f fluorescence responses to changes in membrane potential during whole-cell recording and Ca^{2+} perfusion after cell unroofing. (A and F) TIRF micrographs of cotransfected HEK 293A cells showing Orai1-GCaMP6f (A) and mCherry-STIM1 (F) before pipette break-in. The image intensities have been increased threefold with respect to B–E and G–J to facilitate comparison. (B, C, G, and H) TIRF images of Orai1-GCaMP6f (B) and mCherry-STIM1 (G) at +20 mV holding potential and during -100 mV test pulse (C and H). (D, E, I, and J) TIRF images of the same cell after mechanical unroofing showing Orai1-GCaMP6f and mCherry-STIM1 upon perfusion of solutions containing (D and I) and lacking (E and J) 2 mM Ca^{2+} . Scale bar in J is 20 μm (applies to A–I). (K–M) Plots of whole-cell current (K), Orai1-GCaMP6f fluorescence (L), and mCherry-STIM1 (M) fluorescence in response to test pulses to -40 and -100 mV. Note the parallel changes in Orai1-GCaMP6f current and fluorescence during test pulses and the lack of change in mCherry-STIM1 fluorescence. (N) Comparison of Orai1-GCaMP6f fluorescence at +20 mV holding potential and upon -40 and -100 mV test pulses with Orai1-GCaMP6f fluorescence from the same, subsequently unroofed, cell perfused with solutions containing (2 Ca) and lacking (0 Ca) 2 mM Ca^{2+} . Data are representative of six cells acquired over 4 d. Images and traces correspond to cell E (see Fig. S3).

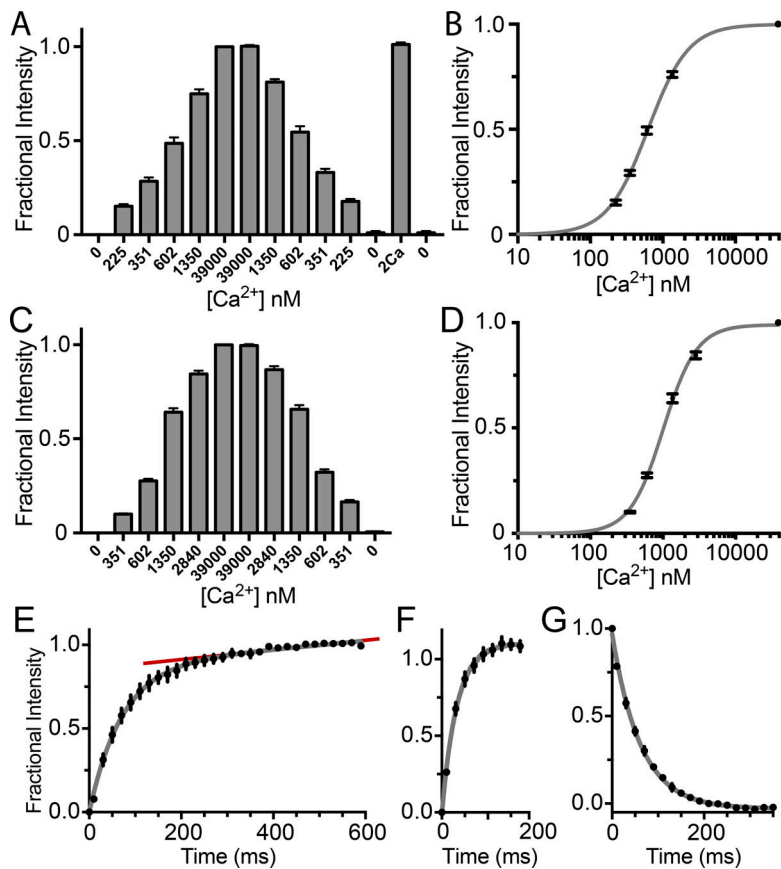


Figure 3. Measurement of Orai1-GECI affinity and kinetics. HEK 293A cells were cotransfected with Orai1-GCaMP6f and mCherry-STIM1, or with Orai1-G-GECO 1.2 and mCherry-STIM1. ER Ca²⁺ stores were depleted by whole-cell break-in and dialysis with pipette solutions containing IP₃. **(A–D)** Unroofed cells were sequentially perfused with buffered Ca²⁺ solutions in the order indicated and imaged by TIRF microscopy. **(A and B)** Orai1-GCaMP6f in situ binding affinity. **(A)** Normalized Orai1-GCaMP6f fluorescence from the cell footprint. Note the lack of photobleaching of Orai1-GCaMP6f. **(B)** Corresponding association curve, fitted by the Hill equation with K_d of 620 nM and an hc of 1.56 (gray line; $R^2 = 0.993$). 95% CIs were 590–660 nM for the K_d and 1.44–1.68 for the hc . $n = 7$ cells acquired over 3 d. **(C and D)** Orai1-G-GECO 1.2 in situ binding affinity. Normalized Orai1-G-GECO 1.2 fluorescence from the cell footprint (C) and association curve (D), fitted by the Hill equation with K_d of 1,010 nM and hc of 1.88 (gray line; $R^2 = 0.994$). 95% CIs were 950–1,070 nM for the K_d and 1.74–2.05 for the hc . $n = 6$ cells acquired over 2 d. **(E–G)** Orai1-GCaMP6f fluorescence rise and fall kinetics during whole-cell recording. $n = 6$ cells. **(E)** Rising phase of Orai1-GCaMP6f fluorescence in response to a 600-ms test pulse to -100 mV in 2 mM extracellular Ca²⁺. The gray line, representing the time course of Ca²⁺ association with the tethered GCaMP6f probe, indicates a fit to the sum of a single exponential association with a time constant of 71 ms and a linear rising function ($R^2 = 0.949$). The red line indicates the linear component of the rising phase. Half-rise time was 49 ms (43–56 ms, 95% CI). **(F)** Mean rising phase Orai1-GCaMP6f fluorescence of HEK 293A cells in response to a 600-ms test pulse to -100 mV in 20 mM extracellular Ca²⁺. Gray line indicates the fit to a single exponential association function with a time constant of 33 ms ($R^2 = 0.961$). **(G)** Mean falling phase of Orai1-GCaMP6f fluorescence of HEK 293A cells upon stepping back to +20 mV from -100 mV in 2 mM extracellular Ca²⁺. Gray line indicates a single exponential decay function with a time constant of 62 ms ($R^2 = 0.989$). Half-fall time was 43 ms (41–45 ms, 95% CI). Error bars are \pm SEM.

The procedure is referred to here as “mechanical unroofing,” analogous to unroofing with a sonicator (Gordon et al., 2016, 2018; Zagotta et al., 2016). Following mechanical unroofing, superfusion of solutions containing varying [Ca²⁺] demonstrated that the GCaMP6f indicators tethered to Orai1 in the basal PM remained highly responsive to Ca²⁺, even after imaging fluorescence responses to eight or more protocols during whole-cell recording. The pattern of mCherry-STIM1, like Orai1-GCaMP6f, was typically well preserved after unroofing, indicating substantial retention of ER–PM junctions. Moreover, comparison of unroofed cell fluorescence intensities in saturating Ca²⁺ concentrations (2 mM) with those from the same cell during whole-cell recording showed that test pulses to -100 mV in 2 mM external Ca²⁺ did not saturate the Orai1-GCaMP6f indicator (Fig. 2 N).

To measure the K_d of Orai1-GCaMP6f for Ca²⁺, standard buffered Ca²⁺ solutions were perfused across unroofed cells while recording TIRF of the basal PM (Fig. 3, A and B). This approach yielded notably consistent results and an excellent fit to the Hill equation. The K_d obtained for Orai1-GCaMP6f was 620 nM with an hc of 1.6. The related, but lower affinity, C-terminal fusion construct Orai1-G-GECO 1.2 had a K_d value of 1,010 nM with $hc = 1.9$ (Fig. 3, C and D). Both tandem probes are suitable for monitoring Orai1 channel activity with potential advantages

of different levels of sensitivity and saturation; for further experiments, we focused on the higher affinity GCaMP6f indicator.

Defining the kinetic properties of Orai1-GCaMP6f is also necessary to interpret dynamic fluorescence traces in relation to channel activity. Rise and fall rates were measured during whole-cell recording at varying external [Ca²⁺] and test potentials, as illustrated in Fig. 3, E–G and summarized in Table 3. Because the Ca²⁺ probes are tethered to the low-conductance hexameric Orai1 channel, the time course of fluorescence rise upon hyperpolarization would include Ca²⁺ influx, binding of up to four Ca²⁺ ions to the calmodulin portion of GCaMP6f, and subsequent conformational changes leading to fluorescence emission. For cells held in extracellular solutions containing 2 mM Ca²⁺, the fluorescence rise was well-fitted by a curve composed of an exponential and a linear component (Fig. 3 E). In this case, the rise time constant (τ_{Rise}) was 71 ms. The rise time was approximately twice as fast on average after elevating extracellular Ca²⁺ to 20 mM ($\tau_{\text{Rise}} = 33$ ms; Fig. 3 F and Table 3). Upon return to the +20-mV holding potential at which influx is negligible, the fall time should reflect clearance of local Ca²⁺ and unbinding of Ca²⁺ from the probe leading to loss of fluorescence. This process was well fitted by a declining single exponential curve (Fig. 3 G), with a fall time constant of 62 ms in 2 mM Ca²⁺ extracellular solution, and was largely unaffected by increasing

Table 3. Orai-GCaMP6f fluorescence rise/fall kinetics

[Ca ²⁺] mM	Pulse mV	Rise τ_{Rise} ms	95% CI	Fall τ_{Fall} ms	95% CI
20	-100	33	28–38	63	60–67
2	-100	71	62–80	62	58–65
0.6	-100	86	72–103	50	44–58
2	-100	81	69–95	59	53–66
2	-70	96	80–116	55	48–62
2	-40	91	61–141	46	34–62

Changes in Orai1-GCaMP6f fluorescence were recorded in response to test pulses and varying external [Ca²⁺]. $n = 6$ cells acquired over 4 d. τ_{Fall} , fall time constant.

external Ca²⁺ (Table 3). Taken together, these measurements define the affinity and kinetics of Orai1-tethered GCaMP6f and help to define a response function that translates Orai1-GCaMP6f fluorescence traces into current traces.

Correspondence between Orai1-GCaMP6f fluorescence and Ca²⁺ current

To assess the suitability of Orai1-GCaMP6f for monitoring a range of Orai1 current levels, we applied steps to increasingly negative membrane potentials. Orai1-GCaMP6f current (Fig. 4 A) and fluorescence (Fig. 4 B) rose progressively in response to increasing voltage steps to hyperpolarized potentials. As expected from probe response times, changes in fluorescence were not immediate but took 100–300 ms to approach plateau values. Plots of Orai1-GCaMP6f plateau fluorescence and voltage revealed that the shapes of the I-V and F-V curves are similar (Fig. 4, C and D). In this case, whole-cell fluorescence was calculated by multiplying the integrated fluorescence from the PM footprint by the ratio of the total PM surface area, determined by measuring the whole-cell membrane capacitance, to the imaged cell footprint area. The number of Ca²⁺ ions conducted per photon emitted by Orai1-GCaMP6f is then given by the simple ratio between the mean current (in Ca²⁺ ions per second) and fluorescence (in photons per second) at the plateau of the response, resulting in an estimate of 65 ± 2 Ca²⁺ ions per photon emitted ($n = 3$ cells) at -100 mV.

We sought to identify a mathematical function to describe the steady-state relationship between whole-cell current and fluorescence. A simple model is that whole-cell responses are entirely accounted for by the properties of the Orai1-GCaMP6f protein itself, which we defined under steady-state conditions by imaging unroofed cells perfused with buffered Ca²⁺ solutions (Fig. 3, A and B). Plateau F and I measurements from Fig. 4, C and D, were replotted as a scatterplot (Fig. 4, E and F); since the current output of all three cells was similar, F-I values were fitted to the Hill equation. Individual F-I values lay quite close to the lower portion of the fitted curve ($R^2 = 0.992$), which had an hc of 1.6. The Hill equation produced a better fit of the F-I data than linear regression, with residuals that were more symmetrically distributed around the fitted curve (Fig. S1, A and B). This analysis was extended to individual test pulses and all six cells by normalizing F-I values using the current produced by each

cell at -40 mV, a driving force that doesn't elicit fast Ca²⁺-dependent inactivation (Fig. 2 K and Fig. 4 A). Normalized F-I values were also well-fitted by the Hill equation with a similar hc (Fig. S1, C and D). When F-I values from stepped test pulses were similarly normalized, the fitted Hill equation curve was nearly identical to the curve derived from individual test pulses. Taken together, this analysis indicates that Orai1-GCaMP6f responses are consistent across cells and across different test pulse protocols and are governed by a Hill equation with $hc = 1.6$, just like Orai1-GCaMP6f in unroofed cells. Therefore, whole-cell responses can be accounted for by the properties of the Orai1-GCaMP6f protein itself; this strongly suggests that any other Ca²⁺-permeable ion channels that might be present in HEK 293A cells do not appreciably contribute to Orai1-GCaMP6f responses.

Varying external Ca²⁺ concentration produced different patterns of correspondence between Orai1-GCaMP6f current and fluorescence during hyperpolarizing test pulses (Fig. 4, G and H). Magnitudes of Orai1-GCaMP6f currents were similar at 600 μM and 200 μM external [Ca²⁺], whereas fluorescence varied in direct proportion to external [Ca²⁺]. The difference in proportionality can be explained by the contribution of Na⁺ current at low external Ca²⁺ concentrations, calculated with a known half-maximal effective concentration and hc for Ca²⁺ block of monovalent current (Yen et al., 2016) through the Orai1 channel. At elevated external [Ca²⁺] (20 mM), inactivation of current was pronounced, and fluorescence was elevated before and after the pulse. Taken together, these studies establish that Orai1-GCaMP6f is a rapid and reliable fluorescence reporter of Orai1 Ca²⁺ influx, with a known steady-state response function and an appropriate Ca²⁺ affinity for detecting Orai1 Ca²⁺ signals of different magnitudes.

STIM1-Orai1 puncta are functionally heterogeneous

Having established correspondence between Orai1-GCaMP6f fluorescence and current in normal Ringer, we next used the Patch-TIRF approach to ask whether Orai1 channel activity differs between puncta within the same cell (Fig. 5). After break-in and store depletion, the spatial patterns of fluorescence from mCherry-STIM1 and Orai1-GCaMP6f were similar (Fig. 5, A and B). At most puncta, Orai1-GCaMP6f fluorescence increased during a hyperpolarizing test pulse to -100 mV; however, at some puncta, Ca²⁺ entry was not detected (Fig. 5 C, white

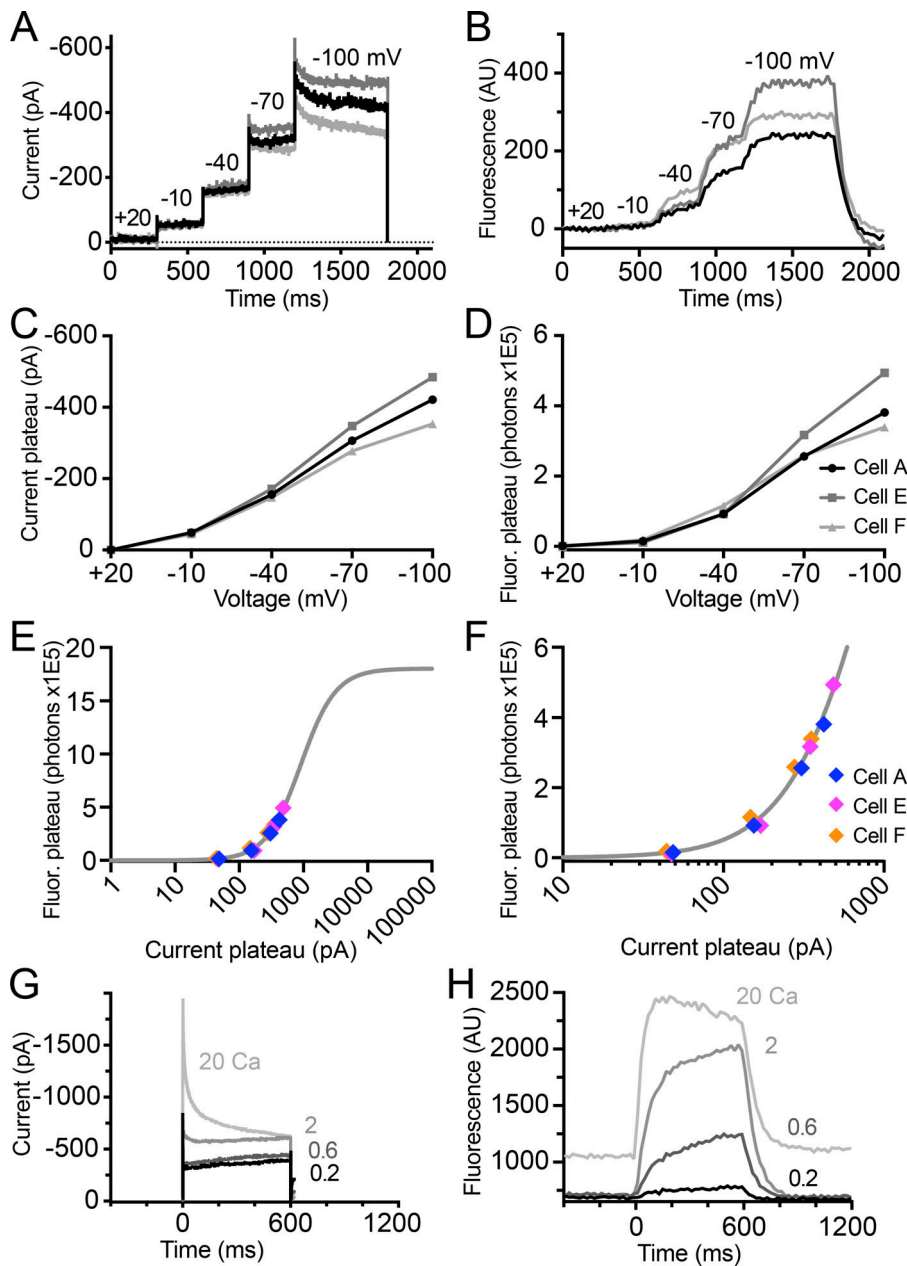


Figure 4. **Orai1-GCaMP6f current and fluorescence in response to changes in membrane potential and external Ca^{2+} .** (A and B) Whole-cell currents (A) and Orai1-GCaMP6f fluorescence (B) in response to a series of steps to increasingly negative membrane potential in 2 mM external Ca^{2+} . Membrane potentials are indicated above the traces. Data from three different cells. (C and D) Plots of Orai1-GCaMP6f whole-cell current (C) and fluorescence (D) for the same three cells as a function of test potential in 2 mM external Ca^{2+} . (E and F) Scatterplots of whole-cell current versus fluorescence (colored diamonds) for the same three cells with fitting to the Hill equation (gray line; $R^2 = 0.992$ and $hc = 1.6$ with 95% CI of 1.2–2.2). (F) Enlargement of lower central portion of E. (G and H) Plots of Orai1-GCaMP6f whole-cell current (G) and fluorescence (H) in response to a series of 600 ms duration -100 mV test pulses at increasing external Ca^{2+} concentrations. External Ca^{2+} concentration in mM are indicated beside the traces. G and H correspond to cell E (see Fig. S3). AU, arbitrary unit.

arrowheads). Orai1 channel activity was mapped across the cell by calculating the change in Orai1-GCaMP6f fluorescence ($\Delta F/F_0$) at each pixel (Fig. 5 D). $\Delta F/F_0$ was lower in the corners of the cell and higher at particular puncta, especially along the edges of the cell footprint. For the most part, $\Delta F/F_0$ values changed smoothly across the interior of the footprint.

Puncta also exhibited differences in the kinetics of Orai1-GCaMP6f responses. Kinetic properties of individual puncta were mapped across the cell footprint using an A-index (Fig. 5 E), defined as the fluorescence from the first 200 ms of a 600 ms test pulse divided by the fluorescence from the last 200 ms. Upon stepping from +20 to -100 mV, whole-cell current increased abruptly then increased in a slow phase lasting hundreds of milliseconds (Fig. 5 F). Orai1-GCaMP6f fluorescence rose rapidly in most individual puncta (Fig. 5 G). However, Orai1-GCaMP6f fluorescence at some puncta rose much more

slowly over hundreds of milliseconds, resulting in a smaller A-index (Fig. 5 H and corresponding orange arrowhead in Fig. 5 E).

As an alternative approach to measure and compare puncta channel activity, we automated puncta identification and recording using a particle tracking program (TrackMate; Fig. S2). Particle tracking enabled individual fluorescently labeled puncta to be followed even in the presence of small shifts in position that occur between different fluorescence channels or upon cell unroofing. Orai1-GCaMP6f (Fig. S2, A and C) and mCherry-STIM1 (Fig. S2, B and D) TIRF image stacks acquired during test pulses were concatenated, and puncta position and fluorescence intensity were tracked in every frame. The identified positions of Orai1-GCaMP6f and mCherry-STIM1 foci (Fig. S2 E) were tightly clustered and clearly associated with the same punctum (Fig. S2 F). A similar arrangement of puncta was

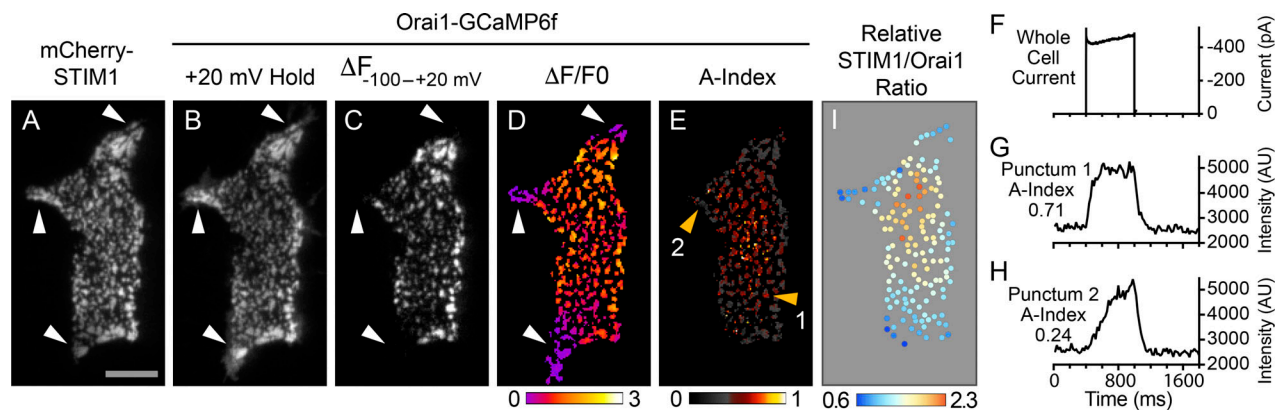


Figure 5. Orai1-GCaMP6f activity differs between puncta. HEK 293A cells were cotransfected with Orai1-GCaMP6f and mCherry-STIM1. **(A and B)** TIRF micrographs of mCherry-STIM1 (A) and Orai1-GCaMP6f (B) fluorescence at +20 mV holding potential. **(C)** Difference between Orai1-GCaMP6f fluorescence at -100 and +20 mV. White arrowheads in A–D indicate puncta with little or no change in fluorescence. **(D)** Map of Orai1-GCaMP6f plateau $\Delta F/F_0$ upon stepping from +20 to -100 mV. **(E)** Map of A-index. Orange arrowheads indicate puncta with high (1) and low (2) A-indices. **(F)** Whole-cell current for the cell shown in (A–E). **(G and H)** Orai1-GCaMP6f fluorescence traces corresponding to puncta 1 and 2. **(I)** Map of relative STIM1/Orai1 ratio; each circle represents an individual punctum. Scale bar in A is 10 μm , applies to B–E and I. Images and trace correspond to cell B (see Fig. S3).

obtained using SRRF computational superresolution of mCherry-STIM1 (Fig. S2 G). Automated recording of Orai1-GCaMP6f (Fig. S2, H and J) and mCherry-STIM1 (Fig. S2, I and K) produced Orai1-GCaMP6f $\Delta F/F_0$ traces (Fig. S2 M) that paralleled manually processed traces (Fig. S2 N) and reached a similar magnitude as pixel-based $\Delta F/F_0$ image maps (Fig. S2 L). As a side note, diffuse fluorescence from Orai1-GCaMP6f, but not mCherry-STIM1 or distinct puncta, were observed in lamellipodia flanking the TIRF footprint (Fig. S2, A and B). On average, ~ 100 puncta were recorded from each cell during a single test pulse (Fig. S3), and results using either manual or automated tracking were congruent.

The ratio of STIM1 to Orai1 is a key determinant of Orai1 channel properties (Hoover and Lewis, 2011; Scrimgeour et al., 2009; Yen and Lewis, 2018), and so we sought to establish whether this factor could account for the observed differences in channel activity and activation rate between puncta. mCherry-STIM1 and Orai1-GCaMP6f resting fluorescence were used as relative measures of the number of STIM1 molecules and Orai1-GCaMP6f channels per puncta. Orai1-GCaMP6f can serve as a stable measure of channel number because puncta $[\text{Ca}^{2+}]$ is low at +20 mV resting potential, and the indicator is relatively insensitive to small differences in $[\text{Ca}^{2+}]$ at the lowest portion of the Ca^{2+} binding curve. Moreover, Orai1-GCaMP6f resting fluorescence was obtained from cells under electrophysiological control during patch clamping and in the presence of strong Ca^{2+} buffering due to the 12 mM EGTA internal solution. We validated electrophysiological control of ionic currents by monitoring Orai1-GCaMP6f resting fluorescence over time (Fig. S4, A–C). Resting fluorescence from cell footprints was quite stable over time (Fig. S4 A), as was resting fluorescence from individual puncta (Fig. S4, B and C). Collectively, puncta resting fluorescence varied with an SD of only 3.6% (Fig. S4 C). The stability of Orai1-GCaMP6f resting fluorescence demonstrates control of PM ion currents and validates use of this value as a measure of relative channel number and as a stable baseline for measurements of channel activity as $\Delta F/F_0$. In addition, the lack of

fluctuation indicates that any nearby Ca^{2+} -permeable organellar channels do not contribute to Orai1-GCaMP6f fluorescence measurements.

Stable Orai1-GCaMP6f resting fluorescence enabled reliable determination of relative, uncalibrated STIM1/Orai1 ratio measurements at puncta. Puncta STIM1/Orai1 ratio varied with a SD of only 3.8% (Fig. S4 D), similar to the stability of Orai1-GCaMP6f resting fluorescence. Relative STIM1/Orai1 ratio did not decrease detectably across the four test pulses, indicating that this measure is relatively resistant to photobleaching under our acquisition conditions.

Relative STIM1/Orai1 ratios were visualized using bubble plots in which bubble size was held constant and STIM1/Orai1 ratio was color-coded, which allowed mapping of puncta properties independent of puncta morphology and fluorescence intensity (Fig. 5 I). There was a general correspondence between $\Delta F/F_0$, A-index, and STIM1/Orai1 ratio; all are lower in puncta near the edges of the cell. Fig. 6 extends the analysis of heterogeneity of Orai1 fluorescence responses and STIM1/Orai1 ratio to five additional cells. Both $\Delta F/F_0$ (Fig. 6, A–E) and A-index values (Fig. 6, F–J) were generally higher in the center of the footprint and lower near the corners. Examination of corresponding bubble plots (Fig. 6, K–O) also revealed systematic patterning of STIM1/Orai1 ratio. The relative STIM1/Orai1 ratio was highest in the center of the cell footprint, lower along the edges, and lowest in the corners of the footprint, exhibiting a gradual transition from center to corners. Comparing these maps to corresponding maps of channel activity and activation rate revealed consistent similarities in spatial pattern. Inactive channels were located at puncta with the lowest relative STIM1/Orai1 ratio, typically <1 , in corners of the cell footprint. Slowly activating channels were located at puncta with relative STIM1/Orai1 ratios in the range of 1 to 2, located mostly along the edges of the footprint. Puncta within the broad central region of the footprint had higher A-indices and relative STIM1/Orai1 ratios. The finding that particular STIM1/Orai1 ratios lead to similar channel properties in different cells suggests that measurements

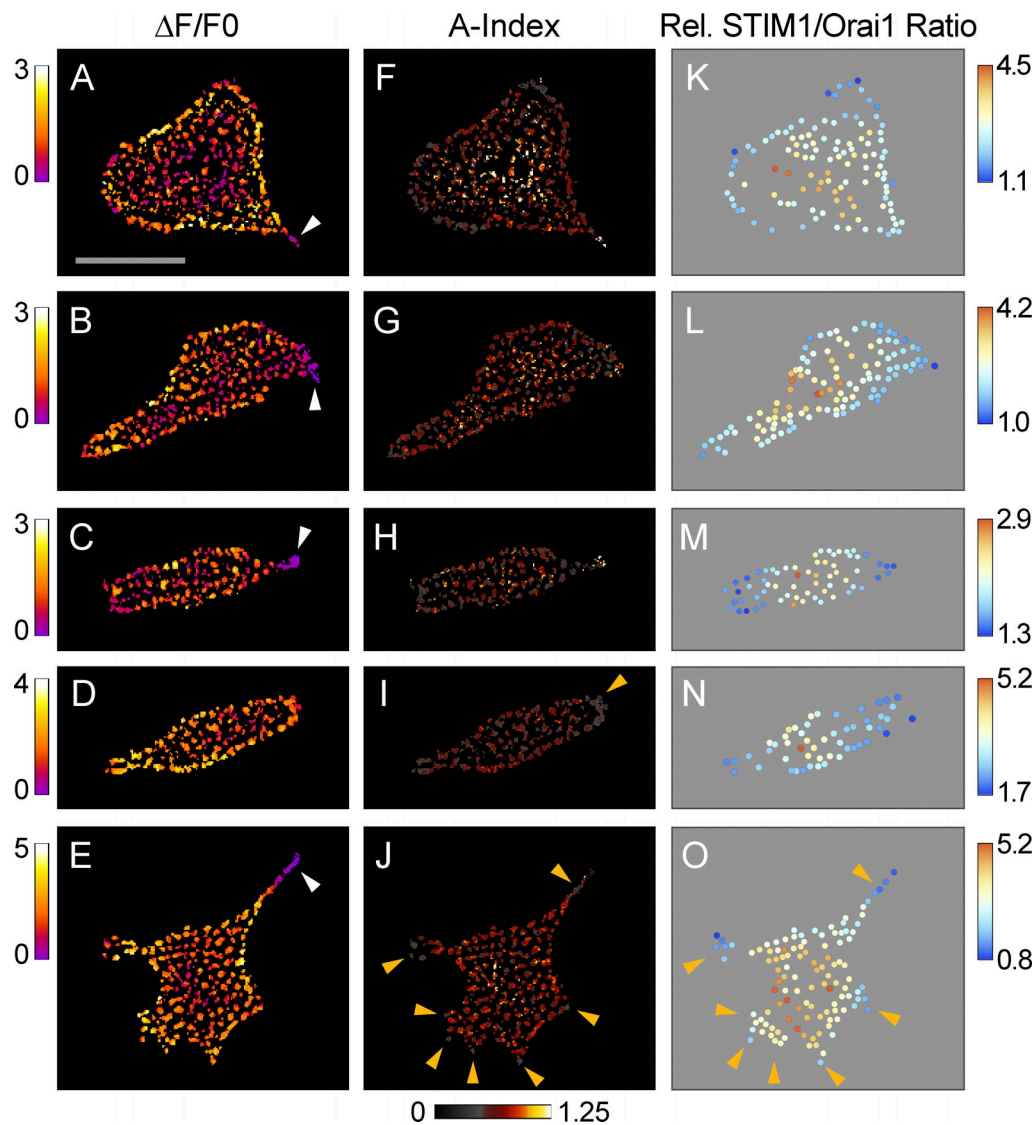


Figure 6. **Correspondence between puncta $\Delta F/F_0$, A-index, and relative STIM1/Orai1 ratio.** Maps of plateau $\Delta F/F_0$ (A–E), A-index (F–J), and relative STIM1/Orai1 ratio (K–O) for five HEK 293A cells cotransfected with Orai1-GCaMP6f and mCherry-STIM1 in response to a 600-ms test pulse to -100 mV in 2 mM extracellular Ca^{2+} . White arrowheads indicate puncta with little or no change in fluorescence in the corners of the cell footprint, and orange arrowheads indicate puncta with and low A-indices. Note that puncta in all seven corners of the cell footprint in J exhibit slow activation of Orai1-GCaMP6f fluorescence. Scale bar in A is 20 μm (applies to B–O). A, F, and K correspond to cell A; B, G, and L to cell C; C, H, and M to cell D; D, I, and N to cell E; and E, J, and O to cell F (see Fig. S3).

of relative STIM1/Orai1 ratio were consistent between cells, which was expected as the same protocol order and acquisition conditions were used for all cells. Taken together, image maps in Fig. 5 and Fig. 6 define spatial patterns of channel activity and kinetic responses across the PM that reflect, in part, the presence of puncta with different STIM1/Orai1 ratios at different parts of the cell.

Orai1 channel activity varies widely between puncta independent of STIM1/Orai1 ratio

We noted that scatterplots of plateau Orai1-GCaMP6f $\Delta F/F_0$ demonstrated substantial variability in channel activity between individual puncta from the same cell (Fig. 7 A). The stability in Orai1-GCaMP6f fluorescence measurements within an

individual trace was measured by comparing fluorescence intensity values occurring near the end of traces after Orai1-GCaMP6f fluorescence had settled back to baseline levels. Pooling of measurements from puncta from cells A–F resulted in a calculated Orai1-GCaMP6f measurement SD of 4.2%, corresponding to a signal-to-noise ratio of 24. Rectangles corresponding to ± 2 SD surrounding the mean were superimposed upon scatterplots of single puncta $\Delta F/F_0$ values (Fig. 7 A). If puncta from a cell exhibited a single set of $\Delta F/F_0$ values arranged in a Gaussian distribution, then 95% of values should lie within two SD of the mean. Instead, most $\Delta F/F_0$ values lie more than two SD away from the mean, indicating that there are, at minimum, several different levels of Orai1-GCaMP6f channel activity in response to a single test pulse to -100 mV.

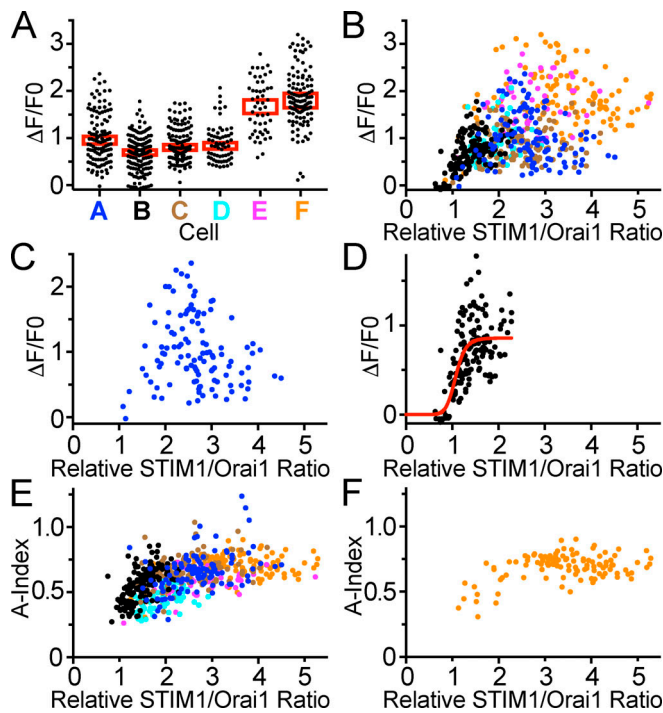


Figure 7. Orai1 channel activity varies widely between puncta independent of STIM1/Orai1 ratio. (A) Plots of Orai1-GCaMP6f $\Delta F/F_0$ plateau values measured in response to a 600-ms test pulse to -100 mV. Red rectangles indicate the mean ± 2 SD of measurement errors. (B) Scatterplot of $\Delta F/F_0$ versus relative STIM1/Orai1 ratio for the six cells shown in A. The cell of origin is indicated by the colored labels shown in A. Note that $\Delta F/F_0$ is near zero only for relative STIM1/Orai1 ratios near 1. (C) Scatterplot of $\Delta F/F_0$ versus relative STIM1/Orai1 ratio shown for cell A. Note the wide spread of values of $\Delta F/F_0$ and relative STIM1/Orai1 ratio for individual puncta from the same cell. (D) Scatterplot of $\Delta F/F_0$ versus relative STIM1/Orai1 ratio shown for cell B. Red line corresponds to a curve fit to the Hill equation ($K_d = 1.08$ [95% CI, 1.02–1.13], $hc = 10$ [95% CI, 6–17], $R^2 = 0.45$). (E) Scatterplot of A-index versus relative STIM1/Orai1 ratio for the six cells shown in A. Inclusion was restricted to puncta with $\Delta F/F_0 > 0.25$. (F) Scatterplot of A-index versus relative STIM1/Orai1 ratio shown for cell F. Note that the A-index declines at low relative STIM1/Orai1 ratios.

The apparently continuous distribution of $\Delta F/F_0$ values strongly suggests that the number of different channel activity levels displayed by Orai1-GCaMP6f puncta is substantially higher.

To determine whether the ratio of STIM1/Orai1 could account for the differing levels of Orai1 channel activity at puncta, we plotted puncta Orai1-GCaMP6f $\Delta F/F_0$ values from the same six cells as a function of mCherry-STIM1/Orai1-GCaMP6f ratio. The resulting distribution was, almost entirely, continuous and independently assorting (Fig. 7 B). For instance, each Orai1-GCaMP6f $\Delta F/F_0$ value between 0.3 and 2–3 corresponded to a wide range of relative STIM1/Orai1 ratios, extending from 1.5 to 4.5. The distribution of responses from an individual cell (Fig. 7 C) was largely similar to the distribution of the entire population (Fig. 7 B). For a given cell, puncta with the most active channels were typically distributed across a broad range of STIM1/Orai1 ratios, but inactive channels were almost entirely found at relative STIM1/Orai1 ratios < 1 . The transition between nonconducting and conducting puncta occurred over a narrow range of relative STIM1/Orai1 ratios (Fig. 7 D), as would be expected from

highly cooperative Orai1 channel opening by STIM1 (Hoover and Lewis, 2011). A plot of $\Delta F/F_0$ as a function of STIM1/Orai1 ratio, from a cell with puncta ratios near the transition point, was fitted to the Hill equation with a K_d of 1.1 and an hc of 10, consistent with high cooperativity. These results show that while Orai1-GCaMP6f channels at puncta are steeply dependent upon a minimum STIM1/Orai1 ratio for channel opening, above a relative ratio of ~ 1.3 , the activity of open Orai1-GCaMP6f channels is largely independent of STIM1/Orai1 ratio.

We next considered whether Orai1-GCaMP6f trace activation time course (A-index) is dependent upon STIM1/Orai1 ratio. Others have noted the existence of a slow phase of channel activation at low STIM1/Orai1 ratios (Hoover and Lewis, 2011; McNally et al., 2012; Scrimgeour et al., 2009). When A-index was plotted as a function of relative STIM1/Orai1-GCaMP6f ratio at puncta, we found that, at low STIM1/Orai1 ratios, A-index increased progressively with increasing STIM1/Orai1 ratio, while at high STIM1/Orai1 ratios, A-index approached a limit distributed around ~ 0.7 (Fig. 7 E). A-indices of puncta with higher relative STIM1/Orai1 ratios, > 2.5 , were largely similar to each other. Puncta from individual cells reflected this general trend (Fig. 7 F).

Single puncta currents and estimation of local cytosolic $[Ca^{2+}]$

Ca^{2+} from Orai1 channels exits into the bulk of the cytoplasm through the puncta margins. The magnitude of this flux in large part determines activation of target proteins outside puncta. In contrast, activation of targets within puncta is determined by the nanoscopic $[Ca^{2+}]$ where these proteins are located. Determining a composite $[Ca^{2+}]$ for a punctum as a whole is an important step in understanding the distribution of free Ca^{2+} within puncta. Using our calibration of the Orai1-GCaMP6f response to varying $[Ca^{2+}]$ in unroofed cells (Fig. 3), we determined single puncta $[Ca^{2+}]$ and current (Fig. 8). Unroofed cell fluorescence measurements were used to calculate and map the fractional saturation of the Orai1-GCaMP6f probe (Fig. 8, A–C) and the $[Ca^{2+}]$ at puncta (Fig. 8, D–F), determined using the K_d and hc of Orai1-GCaMP6f. The median puncta $[Ca^{2+}]$ was 540 nM, with a range of 260–2,600 nM. Single puncta currents were derived by apportioning whole-cell current across the population of puncta within a cell (Fig. 8, G–I). Apportioning was guided by three linked equations, expressed as ratios, that are diagrammed in Fig. S5. First, PM area was used to calculate the current through only those Orai1-GCaMP6f channels present in the TIRF footprint. Second, Orai1-GCaMP6f fluorescence was used to calculate the current through only those puncta that were automatically identified (i.e., tracked). Third, the tracked puncta current, determined in step two, was apportioned across puncta based upon the product of puncta $[Ca^{2+}]$ (proportional to channel activity) and resting Orai1-GCaMP6f fluorescence (proportional to channel number). Single puncta current calculations yielded a median value of -450 fA with a range of -100 to $-1,900$ fA (Fig. 8 G), corresponding to a mean value of ~ 100 –200 open channels (see Discussion). The range of current values was so large because puncta in Patch-TIRF vary not only in channel activity, but also in size. Maps of puncta Ca^{2+} current (Fig. 8, H and I) show that most Ca^{2+} ions entered through a group of puncta along one edge of the cell footprint.

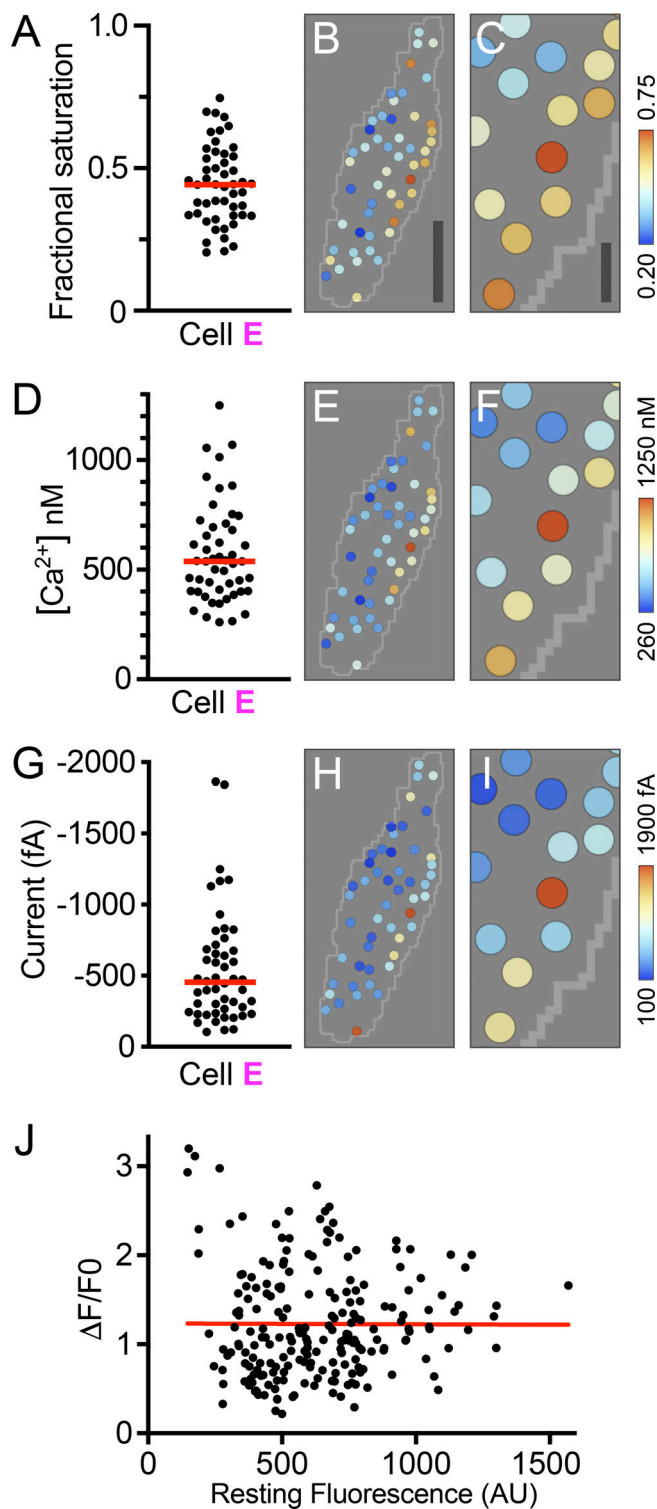


Figure 8. **Measurement of current through individual puncta.** (A) Plot of the plateau fractional saturation of Orai1-GCaMP6f at puncta in cell E during a 600-ms test pulse to -100 mV. Red line indicates the mean. (B) Map of Orai1-GCaMP6f fractional activation at puncta. Light gray line indicates the edge of the cell footprint. (C) Enlargement of central right portion of B. (D) Plot of plateau $[Ca^{2+}]$ at puncta in cell E. Red line indicates the median. (E) Map of plateau $[Ca^{2+}]$ at puncta. (F) Enlargement of central right portion of E. (G) Plot of Orai1 plateau Ca^{2+} current through puncta in cell E. Red line indicates the median. (H) Map of Orai1 plateau Ca^{2+} current at puncta. (I) Enlargement of central right portion of H. (J) Scatterplot of $\Delta F/F_0$ versus resting Orai1-

These calculations assume that Ca^{2+} ions are captured and detected by GCaMP6f proteins positioned near the pore of open Orai1-GCaMP6f channels. In this case, the fluorescence signal from a single open channel would not depend upon the number of surrounding channels in a punctum. Alternatively, larger puncta with more Orai1-GCaMP6f channels might detect a larger fraction of Ca^{2+} ions than would smaller puncta. In this case, fluorescence from a punctum would be a function of both channel activity and puncta size, making calculations of puncta $[Ca^{2+}]$ more uncertain. We assessed whether channel activity was dependent upon the number of channels in puncta by plotting $\Delta F/F_0$ as a function of Orai1-GCaMP6f resting fluorescence (F_0 ; Fig. 8 J). To avoid contributions from largely inactive puncta with low STIM1/Orai1 ratio, as well as unknown effects of very high STIM1/Orai1 ratio, we limited our analysis to puncta with relative STIM1/Orai1 ratios from 2 to 3. We found that the fluorescence signal due to channel activity did not depend upon Orai1-GCaMP6f channel number. This analysis supports a model in which Ca^{2+} is detected by GCaMP6f positioned near the channel pore, which, in turn, allows Orai1-GCaMP6f fluorescence to serve as an accurate readout of channel activity and puncta $[Ca^{2+}]$.

Discussion

In puncta, macromolecular clustering of STIM1 and Orai1 leads to opening of Orai1 channels and store-operated Ca^{2+} entry, but many parts of this process remain hidden from view. Here, we characterize a fusion of the Orai1 channel and a genetically encoded Ca^{2+} indicator, Orai1-GCaMP6f, to optically record Orai1 channel activity from individual puncta. Cell-wide mapping of Orai1 channel activity and local Ca^{2+} influx revealed widespread differences between puncta within the same cell. Moreover, simultaneous measurement of mCherry-STIM1 fluorescence uncovered a previously unsuspected STIM1/Orai1 gradient that extends across the cell surface. These findings provide a puncta-level view of Orai1 activity and establish a new experimental platform that facilitates systematic comparisons between puncta composition and activity.

The utility of our experimental approach depends upon the performance of the Orai1-GCaMP6f probe. Orai1 channel properties are unaffected by C-terminal fusion to GCaMP6f, and the fusion's Ca^{2+} affinity is suitable for detecting a wide range of channel activity without saturating. Orai1-GCaMP6f rise and fall kinetics are sufficiently fast to record channel currents that vary on a time scale <100 ms, but not fast Ca^{2+} -dependent inactivation, which possesses a principle decay constant of ~ 10 ms (Hoth and Penner, 1993; Zweifach and Lewis, 1995). The ability to measure channel activity optically presented us with an

GCaMP6f fluorescence intensity (F_0) at individual puncta for all six cells. Puncta STIM1:Orai1 ratio was restricted to values between 2 and 3. Linear curve fit (red line) indicates that puncta $\Delta F/F_0$ is not related to the number of Orai1-GCaMP6f channels at a punctum (slope = -0.00001 , $R^2 = 0.00002$; slope $\neq 0$, $P = 0.95$, F test). Scale bar in B is $10 \mu m$ (applies to E and H), and the scale bar in C is $2.5 \mu m$ (applies to F and I).

opportunity to record channel activity from single puncta. Single puncta Orail-GCaMP6f fluorescence was detected easily, as expected based on our previously recorded Ca^{2+} currents from individual channels using similar fusion probes (Dynes et al., 2016). The high dynamic range of Orail-GCaMP6f, with a single punctum signal-to-noise ratio of 24, independent puncta readout, and a known steady-state response function enable sensitive and quantitative comparisons of channel activity between puncta. Calibration of Orail-GCaMP6f output using fluorescence from unroofed cells allows puncta Ca^{2+} currents to be estimated. This combination of probe characteristics and analytical approaches provides a foundation for relating channel activity to the molecular composition of STIM1-Orail puncta.

Given reports that various membrane proteins and the calcium effector calmodulin are localized at puncta (Chang et al., 2017; Li et al., 2017), as well as selective positioning of Ca^{2+} -dependent transcription factors (Lin et al., 2019) near Orail channels, new techniques to directly measure local Ca^{2+} are needed. Calibration of Orail-GCaMP6f using unroofed cells enabled calculation and mapping of a composite measure of $[\text{Ca}^{2+}]$ at each punctum. To our surprise, the Orail-GCaMP6f probe did not approach saturation in response to strongly hyperpolarizing test pulses. On average, puncta exhibited half-maximal responses to test pulses to -100 mV in 2 mM external Ca^{2+} , corresponding to a Ca^{2+} concentration of 500–600 nM, measured in standard KCl-MOPS buffer used to mimic the ionic composition of the cytosol. Previous calculations, based upon estimates of Orail single-channel current, indicate that the opening of only three channels in a 300-nm-diameter punctum would lead to a similar puncta-wide median $[\text{Ca}^{2+}]$ (Hogan, 2015). Freeze-fracture electron micrographs of HEK 293A cells transfected with high levels of STIM1 and Orail, taken after ER store depletion with thapsigargin, provide an approximate guide to the number of channels per punctum: 200–300 (Perni et al., 2015). We obtained a roughly similar number of open channels (~ 100 –200) by dividing our estimate of median single puncta current, -450 fA in 2 mM external Ca^{2+} , by previous estimates of Orail single channel currents (-1.9 to -3.5 fA, calculated by dividing single channel currents obtained in 20 mM external $[\text{Ca}^{2+}]$ by 2; Prakriya and Lewis, 2002; Yeromin et al., 2004). These calculations point to a large mismatch between the puncta $[\text{Ca}^{2+}]$ derived from the K_d and fractional activation of our Orail-GCaMP6f probe, and the estimated puncta $[\text{Ca}^{2+}]$ produced by the combined current from 100–200 open Orail channels. Many possible explanations can be envisioned including errors in estimates of single-channel current and open probabilities, uncertain assumptions of Ca^{2+} flux modeling, alteration of GCaMP6f function by the composition of our internal solution, or suppression of GCaMP6f responses due to steric hindrance in the crowded cytoplasmic environment of ER-PM junctions. Resolution of this issue awaits further study, but it does not affect the ability to make quantitative comparisons of local Orail-GCaMP6f activity during whole-cell recording.

Studies of STIM1-Orail stoichiometry have prompted a sequential gating model in which progressive binding of STIM1 subunits leads to a series of channel states with increasing Ca^{2+} conductance but different biophysical properties, as reviewed

(Yen and Lewis, 2019). Calibration and measurement of STIM1/Orail ratio indicates that Orail channels can be trapped at STIM1 puncta at STIM1/Orail ratios <1 , but these channels are essentially inactive (Hoover and Lewis, 2011). Higher but still low STIM1/Orail ratios are associated with low-conductance channel states in which Orail currents are carried predominantly by Na^+ in 2 mM external Ca^{2+} as shown by replacing Na^+ with NMDG (McNally et al., 2012), or in which Orail channels lack fast Ca^{2+} -dependent inactivation but instead display a slow phase of channel activation lasting hundreds of milliseconds (Hoover and Lewis, 2011; McNally et al., 2012; Scrimgeour et al., 2009). Even blocking the binding of STIM1 to a single Orail subunit, demonstrated using concatenated hexameric Orail constructs with a single STIM1 binding mutation (L273D), leads to a channel state or states with lower open probability, higher unitary conductance, reduced Ca^{2+} affinity, and altered pore structure, as evidenced by reduced selectivity for Na^+ over Cs^+ in divalent-free external solution (Yen and Lewis, 2018). Therefore, STIM1 needs to bind to all six Orail subunits to produce the classically defined CRAC current. While this work collectively supports a sequential model for Orail channel gating by STIM1, none of these studies assessed channel activity or channel stoichiometry at puncta, the macromolecular structure where gating interactions occur.

Our Patch-TIRF experiments revealed local differences in Orail channel activity and activation time course that point to local differences in Orail channel state. Inactive channels were found at sites with the lowest STIM1/Orail ratio, the corners of some cells, while active channels displaying slow activation were found at sites with slightly higher STIM1/Orail ratios, in the corners of other cells and along the edges of the cell footprint. Orail channels lacking a pronounced slow activation phase were found primarily within the center of the cell footprint, where the STIM1/Orail ratio was highest. Moreover, we can assign actual STIM1/Orail ratios to these relative ratios using a single point of reference. The abrupt transition from a low- to high-conductance state was reported to occur at a STIM1/Orail ratio of 1.8 (Hoover and Lewis, 2011); in our experiments, this transition occurs at a relative ratio of 1.3, and so actual puncta STIM1/Orail ratios can be calculated by multiplying relative ratios by 1.4. The wide range and progressive nature of these STIM1/Orail gradients, together with our calibration procedures, should enable systematic study of the effects of STIM1/Orail ratio on Orail channel gating, activation, and channel state.

Hoover and Lewis (2011) reported that puncta formed by depletion of ER stores with thapsigargin possess similar STIM1/Orail ratios across the cell footprint. However, our Patch-TIRF observations reveal a different spatial pattern. We speculate that differences in the resting distribution of STIM1 and Orail may contribute to the formation of a STIM1/Orail gradient after store depletion. In transfected cells, lamellipodia flanking the cell footprint possess labeled Orail channels but not STIM1-labeled ER before store depletion (Perni et al., 2015); similarly, we observe Orail-GCaMP6f channels in lamellipodia, but not mCherry-STIM1 or distinct puncta, after ER store depletion during whole-cell recording. Therefore, puncta formed near the edges and corners possess larger territories from which to trap Orail

channels diffusing in the PM than more centrally located puncta. If correct, this explanation implies that similar STIM1/Orai1 gradients, with lower ratios at edges and corners, are a consequence of cell morphology and thus may be a common feature of SOCE.

Since cloning of the genes encoding STIM1 and Orai1, many studies have reconstituted or amplified CRAC currents by cellular expression of STIM1 and Orai1, and this approach has enabled great progress in understanding molecular mechanisms of channel gating and activation (Prakriya and Lewis, 2015). However, a common underlying assumption is that puncta composition and channel properties are uniform across the cell. We suggest that currents recorded in some transfection studies might have been affected by the presence of heterogeneous populations of Orai1 channels, including channels with altered properties due to puncta with different STIM1/Orai1 ratios. In the heterogeneous population of puncta we observe in transfected cells, some puncta have STIM1/Orai1 ratios <2:1. Indeed, we can directly observe and map slow channel activation, which is associated with other altered channel properties and is correlated with low puncta STIM1/Orai1 ratio in our experiments. We expect that transfecting higher ratios of STIM1:Orai1, such as 10:1 (Yen and Lewis, 2018), will raise cell-wide STIM1/Orai1 ratios so that no puncta possess a ratio <2:1. Finally, cellular expression of STIM1 and Orai1 leads to another form of puncta heterogeneity, puncta size differences, which is widely if not universally found in transfection experiments (Orci et al., 2009; Várnai et al., 2007). Our analysis reveals that channel activity is unaffected by a sevenfold change in puncta size as long as STIM1/Orai1 ratio is held constant.

Within the same cell, puncta with high STIM1/Orai1 ratios (relative ratio >1.5) exhibited a range of channel activity that appeared unrelated to the stoichiometric requirements for gating. The presence of these activity differences indicates the existence of a subcellular process that controls Orai1 channel activity locally at puncta. While the underlying mechanism is unknown, our cell-wide census of puncta activity provides clues to its functioning. At a given puncta STIM1/Orai1 ratio, channel activity varied by fivefold in an essentially continuous manner and was always above a minimum $\Delta F/F_0$ value of 0.25. While many STIM1 and Orai1 regulatory mechanisms are candidates, such as phosphorylation and binding of other proteins and lipids, to our knowledge none of these mechanisms have been shown produce heterogeneous patterns of channel activity within the cell (Chen et al., 2017; Derler et al., 2016; Srikanth et al., 2013; Walsh et al., 2009). In addition, if this degree of puncta heterogeneity were found in native cells, the range in downstream signaling activity may be wider than currently appreciated.

Previous reports of regional and local expression of SOCE within native cells point to a spatial dimension in the control of Orai1 activity. Certain subcellular structures and organelles exhibit local SOCE, such as invadopodia in WM793 human melanoma cells (Lu et al., 2019), phagosomes in mouse embryonic fibroblasts (Nunes et al., 2012), and immune synapses in human peripheral blood-derived T cells (Lioudyno et al., 2008) and in mouse primary CD4⁺ T cells (Diercks et al., 2018). In addition,

apparently spontaneous local or regional SOCE signals have been detected in mouse astrocytes (Rungta et al., 2016; Toth et al., 2019), human WM793 melanoma cells and umbilical cord endothelial cells (Lu et al., 2019), unstimulated mouse CD4⁺ T cells and Jurkat T cells (Diercks et al., 2018), and mouse CD4⁺ T cells during basal migration in the lymph node (Dong et al., 2017a; Dong et al., 2017b). The mechanisms underlying local control are poorly understood, but STIM1 and/or Orai1 are selectively targeted to subcellular structures that exhibit local SOCE. While local control of Orai1 activity could result from selective depletion of Ca²⁺ from adjacent ER subdomains, local control might also be tied to differences in puncta composition or local signaling mechanisms that target STIM1 or Orai1.

A key difference between our study and previous work is the imaging approach, which enables recording of Orai1 channels in roughly 100 puncta simultaneously. Our plots of Orai1 activity can be used in several ways to understand gating and channel activation. First, they provide data for mathematical modeling of STIM1 binding and Orai1 gating and of Ca²⁺ currents in puncta (Hogan, 2015; Hoover and Lewis, 2011; McIvor et al., 2018; Samanta et al., 2015; Schmidt et al., 2019). Second, they remove uncertainty in stoichiometry when comparing channel activity between experiments. Third, they should be diagnostic for modes of Orai1 regulation. For instance, expression of regulatory proteins that act by sequestering STIM1 or Orai1 should lead to systematic rightward or leftward shifts, respectively, in the STIM1/Orai1 ratio at which the open state transition occurs. In contrast, proteins that selectively alter Orai1 conductance should not affect these parameters. In addition, our mapping will aid in molecular dissection of the poorly understood slow phase of Orai1 channel activation, which acts over hundreds of milliseconds. Finally, the approaches used here can serve as a template for optical recording from other Ca²⁺ permeable channels, and, through the use of genetically encoded sensors for other ions such as H⁺ (Benčina, 2013) or Cl⁻ (Arosio et al., 2010), they might be applied to other classes of ion channels. Taken together, our work ultimately extends the fundamental approach of whole-cell recording to the spatial dimension with submicron resolution.

Acknowledgments

David A. Eisner served as editor.

We thank Amit Jairaman, Medha Pathak, Karinne Németh-Cahalan, James E. Hall, Francesco Tombola, Oswald Steward, and Ian Parker for helpful discussions; and Don Gill and Rich Lewis for troubleshooting assistance.

This work is supported by National Institutes of Health grant R01 NS-14609 to M.D. Cahalan.

The authors declare no competing financial interests.

Author contributions: J.L. Dynes, A.V. Yeromin, and M.D. Cahalan designed the research; J.L. Dynes and A.V. Yeromin performed the experiments and analysis; and J.L. Dynes and M.D. Cahalan wrote the paper.

Submitted: 31 August 2018

Revised: 11 December 2019

Accepted: 21 May 2020

References

- Amcheslavsky, A., M.L. Wood, A.V. Yeromin, I. Parker, J.A. Freites, D.J. Tobias, and M.D. Cahalan. 2015. Molecular biophysics of Orai store-operated Ca²⁺ channels. *Biophys. J.* 108:237–246. <https://doi.org/10.1016/j.bpj.2014.11.3473>
- Arosio, D., F. Ricci, L. Marchetti, R. Gualdani, L. Albertazzi, and F. Beltram. 2010. Simultaneous intracellular chloride and pH measurements using a GFP-based sensor. *Nat. Methods.* 7:516–518. <https://doi.org/10.1038/nmeth.1471>
- Benčina, M. 2013. Illumination of the spatial order of intracellular pH by genetically encoded pH-sensitive sensors. *Sensors (Basel).* 13: 16736–16758. <https://doi.org/10.3390/s131216736>
- Böhm, J., and J. Laporte. 2018. Gain-of-function mutations in STIM1 and ORAI1 causing tubular aggregate myopathy and Stormorken syndrome. *Cell Calcium.* 76:1–9. <https://doi.org/10.1016/j.ceca.2018.07.008>
- Byun, M., A. Abhyankar, V. Lelarge, S. Plancoulaine, A. Palanduz, L. Telhan, B. Boisson, C. Picard, S. Dewell, C. Zhao, et al. 2010. Whole-exome sequencing-based discovery of STIM1 deficiency in a child with fatal classic Kaposi sarcoma. *J. Exp. Med.* 207:2307–2312. <https://doi.org/10.1084/jem.20101597>
- Cahalan, M.D. 2009. STIMulating store-operated Ca(2+) entry. *Nat. Cell Biol.* 11:669–677. <https://doi.org/10.1038/ncb0609-669>
- Chang, C.L., Y.J. Chen, and J. Liou. 2017. ER-plasma membrane junctions: Why and how do we study them? *Biochim. Biophys. Acta Mol. Cell Res.* 1864:1494–1506. <https://doi.org/10.1016/j.bbamcr.2017.05.018>
- Chen, T.W., T.J. Wardill, Y. Sun, S.R. Pulver, S.L. Renninger, A. Baohan, E.R. Schreiter, R.A. Kerr, M.B. Orger, V. Jayaraman, et al. 2013. Ultrasensitive fluorescent proteins for imaging neuronal activity. *Nature.* 499: 295–300. <https://doi.org/10.1038/nature12354>
- Chen, Y.J., C.L. Chang, W.R. Lee, and J. Liou. 2017. RASSF4 controls SOCE and ER-PM junctions through regulation of PI(4,5)P₂. *J. Cell Biol.* 216: 2011–2025. <https://doi.org/10.1083/jcb.201606047>
- Christian, E.P., K.T. Spence, J.A. Togo, P.G. Dargis, and J. Patel. 1996. Calcium-dependent enhancement of depletion-activated calcium current in Jurkat T lymphocytes. *J. Membr. Biol.* 150:63–71. <https://doi.org/10.1007/s002329900030>
- Derler, I., I. Jardin, P.B. Stathopoulos, M. Muik, M. Fahrner, V. Zayats, S.K. Pandey, M. Potesser, B. Lackner, M. Absolonova, et al. 2016. Cholesterol modulates Orai1 channel function. *Sci. Signal.* 9:ra10. <https://doi.org/10.1126/scisignal.aad7808>
- Diercks, B.P., R. Wernser, P. Weidemüller, F. Czarniak, L. Hernandez, C. Lehmann, A. Rosche, A. Krüger, U. Kaufmann, M. Vaeth, et al. 2018. ORAI1, STIM1/2, and RYR1 shape subsecond Ca²⁺ microdomains upon T cell activation. *Sci. Signal.* 11. eaat0358. <https://doi.org/10.1126/scisignal.aat0358>
- Dong, T.X., S. Othy, M.L. Greenberg, A. Jairaman, C. Akunwafo, S. Leverrier, Y. Yu, I. Parker, J.L. Dynes, and M.D. Cahalan. 2017a. Intermittent Ca(2+) signals mediated by Orai1 regulate basal T cell motility. *eLife.* 6:e27827.
- Dong, T.X., S. Othy, A. Jairaman, J. Skupsky, A. Zavala, I. Parker, J.L. Dynes, and M.D. Cahalan. 2017b. T-cell calcium dynamics visualized in a ratiometric tdTomato-GCaMP6f transgenic reporter mouse. *eLife.* 6: e32417. <https://doi.org/10.7554/eLife.32417>
- Dynes, J.L., A. Amcheslavsky, and M.D. Cahalan. 2016. Genetically targeted single-channel optical recording reveals multiple Orai1 gating states and oscillations in calcium influx. *Proc. Natl. Acad. Sci. USA.* 113:440–445. <https://doi.org/10.1073/pnas.1523410113>
- Ellefsen, K.L., J.L. Dynes, and I. Parker. 2015. Spinning-Spot Shadowless TIRF Microscopy. *PLoS One.* 10. e0136055. <https://doi.org/10.1371/journal.pone.0136055>
- Feske, S. 2009. ORAI1 and STIM1 deficiency in human and mice: roles of store-operated Ca²⁺ entry in the immune system and beyond. *Immunol. Rev.* 231:189–209. <https://doi.org/10.1111/j.1600-065X.2009.00818.x>
- Feske, S. 2019. CRAC channels and disease - From human CRAC channelopathies and animal models to novel drugs. *Cell Calcium.* 80:112–116. <https://doi.org/10.1016/j.ceca.2019.03.004>
- Feske, S., Y. Gwack, M. Prakriya, S. Srikanth, S.H. Puppel, B. Tanasa, P.G. Hogan, R.S. Lewis, M. Daly, and A. Rao. 2006. A mutation in Orai1 causes immune deficiency by abrogating CRAC channel function. *Nature.* 441:179–185. <https://doi.org/10.1038/nature04702>
- Fukushima, M., T. Tomita, A. Janoshazi, and J.W. Putney. 2012. Alternative translation initiation gives rise to two isoforms of Orai1 with distinct plasma membrane mobilities. *J. Cell Sci.* 125:4354–4361. <https://doi.org/10.1242/jcs.104919>
- Gao, X., J. Xia, F.M. Munoz, M.T. Manners, R. Pan, O. Meucci, Y. Dai, and H. Hu. 2016. STIMs and Orai1 regulate cytokine production in spinal astrocytes. *J. Neuroinflammation.* 13:126. <https://doi.org/10.1186/s12974-016-0594-7>
- Gordon, S.E., E.N. Senning, T.K. Aman, and W.N. Zagotta. 2016. Transition metal ion FRET to measure short-range distances at the intracellular surface of the plasma membrane. *J. Gen. Physiol.* 147:189–200. <https://doi.org/10.1085/jgp.201511530>
- Gordon, S.E., M. Munari, and W.N. Zagotta. 2018. Visualizing conformational dynamics of proteins in solution and at the cell membrane. *eLife.* 7. e37248.
- Gustafsson, N., S. Culley, G. Ashdown, D.M. Owen, P.M. Pereira, and R. Henriques. 2016. Fast live-cell conventional fluorophore nanoscopy with ImageJ through super-resolution radial fluctuations. *Nat. Commun.* 7:12471. <https://doi.org/10.1038/ncomms12471>
- Hogan, P.G. 2015. The STIM1-ORAI1 microdomain. *Cell Calcium.* 58:357–367. <https://doi.org/10.1016/j.ceca.2015.07.001>
- Hoover, P.J., and R.S. Lewis. 2011. Stoichiometric requirements for trapping and gating of Ca²⁺ release-activated Ca²⁺ (CRAC) channels by stromal interaction molecule 1 (STIM1). *Proc. Natl. Acad. Sci. USA.* 108: 13299–13304. <https://doi.org/10.1073/pnas.1101664108>
- Hoth, M., and R. Penner. 1992. Depletion of intracellular calcium stores activates a calcium current in mast cells. *Nature.* 355:353–356. <https://doi.org/10.1038/355353a0>
- Hoth, M., and R. Penner. 1993. Calcium release-activated calcium current in rat mast cells. *J. Physiol.* 465:359–386. <https://doi.org/10.1113/jphysiol.1993.sp019681>
- Hsieh, T.S., Y.J. Chen, C.L. Chang, W.R. Lee, and J. Liou. 2017. Cortical actin contributes to spatial organization of ER-PM junctions. *Mol. Biol. Cell.* 28:3171–3180. <https://doi.org/10.1091/mbc.e17-06-0377>
- Jaqaman, K., D. Loerke, M. Mettlen, H. Kuwata, S. Grinstein, S.L. Schmid, and G. Danuser. 2008. Robust single-particle tracking in live-cell time-lapse sequences. *Nat. Methods.* 5:695–702. <https://doi.org/10.1038/nmeth.1237>
- Kraft, R. 2015. STIM and ORAI proteins in the nervous system. *Channels (Austin).* 9:245–252. <https://doi.org/10.1080/19336950.2015.1071747>
- Kwon, J., H. An, M. Sa, J. Won, J.I. Shin, and C.J. Lee. 2017. Orai1 and Orai3 in Combination with Stim1 Mediate the Majority of Store-operated Calcium Entry in Astrocytes. *Exp. Neurobiol.* 26:42–54. <https://doi.org/10.15607/en.2017.26.1.42>
- Lacruz, R.S., and S. Feske. 2015. Diseases caused by mutations in ORAI1 and STIM1. *Ann. N. Y. Acad. Sci.* 1356:45–79. <https://doi.org/10.1111/nyas.12938>
- Lepple-Wienhues, A., and M.D. Cahalan. 1996. Conductance and permeation of monovalent cations through depletion-activated Ca²⁺ channels (ICRAC) in Jurkat T cells. *Biophys. J.* 71:787–794. [https://doi.org/10.1016/S0006-3495\(96\)79278-0](https://doi.org/10.1016/S0006-3495(96)79278-0)
- Lewis, R.S. 2011. Store-operated calcium channels: new perspectives on mechanism and function. *Cold Spring Harb. Perspect. Biol.* 3. a003970. <https://doi.org/10.1101/cshperspect.a003970>
- Lewis, R.S., and M.D. Cahalan. 1989. Mitogen-induced oscillations of cytosolic Ca²⁺ and transmembrane Ca²⁺ current in human leukemic T cells. *Cell Regul.* 1:99–112. <https://doi.org/10.1091/mbc.1.1.99>
- Li, X., G. Wu, Y. Yang, S. Fu, X. Liu, H. Kang, X. Yang, X.C. Su, and Y. Shen. 2017. Calmodulin dissociates the STIM1-Orai1 complex and STIM1 oligomers. *Nat. Commun.* 8:1042. <https://doi.org/10.1038/s41467-017-01135-w>
- Lin, Y.P., D. Bakowski, G.R. Mirams, and A.B. Parekh. 2019. Selective recruitment of different Ca²⁺-dependent transcription factors by STIM1-Orai1 channel clusters. *Nat. Commun.* 10:2516. <https://doi.org/10.1038/s41467-019-10329-3>
- Lioudyno, M.I., J.A. Kozak, A. Penna, O. Safrina, S.L. Zhang, D. Sen, J. Roos, K.A. Stauderman, and M.D. Cahalan. 2008. Orai1 and STIM1 move to the immunological synapse and are up-regulated during T cell activation. *Proc. Natl. Acad. Sci. USA.* 105:2011–2016. <https://doi.org/10.1073/pnas.0706122105>
- Lu, F., J. Sun, Q. Zheng, J. Li, Y. Hu, P. Yu, H. He, Y. Zhao, X. Wang, S. Yang, et al. 2019. Imaging elemental events of store-operated Ca²⁺ entry in invading cancer cells with plasmalemmal targeted sensors. *J. Cell Sci.* 132. jcs224923. <https://doi.org/10.1242/jcs.224923>
- Luik, R.M., M.M. Wu, J. Buchanan, and R.S. Lewis. 2006. The elementary unit of store-operated Ca²⁺ entry: local activation of CRAC channels by STIM1 at ER-plasma membrane junctions. *J. Cell Biol.* 174:815–825. <https://doi.org/10.1083/jcb.200604015>
- McCarl, C.A., C. Picard, S. Khalil, T. Kawasaki, J. Röther, A. Papolos, J. Kutok, C. Hivroz, F. Ledest, K. Plogmann, et al. 2009. ORAI1 deficiency and lack of store-operated Ca²⁺ entry cause immunodeficiency, myopathy,

- and ectodermal dysplasia. *J. Allergy Clin. Immunol.* 124:1311–1318.e7. <https://doi.org/10.1016/j.jaci.2009.10.007>
- McCarl, C.A., S. Khalil, J. Ma, M. Oh-hora, M. Yamashita, J. Roether, T. Kawasaki, A. Jairaman, Y. Sasaki, M. Prakriya, et al. 2010. Store-operated Ca²⁺ entry through ORAI1 is critical for T cell-mediated autoimmunity and allograft rejection. *J. Immunol.* 185:5845–5858. <https://doi.org/10.4049/jimmunol.1001796>
- McIvor, E., S. Coombes, and R. Thul. 2018. Three-dimensional spatio-temporal modelling of store operated Ca²⁺ entry: Insights into ER refilling and the spatial signature of Ca²⁺ signals. *Cell Calcium.* 73:11–24. <https://doi.org/10.1016/j.ceca.2018.03.006>
- McNally, B.A., A. Somasundaram, M. Yamashita, and M. Prakriya. 2012. Gated regulation of CRAC channel ion selectivity by STIM1. *Nature.* 482: 241–245. <https://doi.org/10.1038/nature10752>
- Misceo, D., A. Holmgren, W.E. Louch, P.A. Holme, M. Mizobuchi, R.J. Morales, A.M. De Paula, A. Stray-Pedersen, R. Lyle, B. Dalhus, et al. 2014. A dominant STIM1 mutation causes Stormorken syndrome. *Hum. Mutat.* 35:556–564. <https://doi.org/10.1002/humu.22544>
- Morin, G., N.O. Bruechle, A.R. Singh, C. Knopp, G. Jedraszak, M. Elbracht, D. Brémond-Gignac, K. Hartmann, H. Sevestre, P. Deutz, et al. 2014. Gain-of-Function Mutation in STIM1 (P.R304W) Is Associated with Stormorken Syndrome. *Hum. Mutat.* 35:1221–1232. <https://doi.org/10.1002/humu.22621>
- Neher, E., and A. Marty. 1982. Discrete changes of cell membrane capacitance observed under conditions of enhanced secretion in bovine adrenal chromaffin cells. *Proc. Natl. Acad. Sci. USA.* 79:6712–6716. <https://doi.org/10.1073/pnas.79.21.6712>
- Nesin, V., G. Wiley, M. Kousi, E.C. Ong, T. Lehmann, D.J. Nicholl, M. Suri, N. Shahrizaila, N. Katsanis, P.M. Gaffney, et al. 2014. Activating mutations in STIM1 and ORAI1 cause overlapping syndromes of tubular myopathy and congenital myosis. *Proc. Natl. Acad. Sci. USA.* 111:4197–4202. <https://doi.org/10.1073/pnas.1312520111>
- Nunes, P., D. Cornut, V. Bochet, U. Hasler, M. Oh-Hora, J.M. Waldburger, and N. Demaurex. 2012. STIM1 juxtaposes ER to phagosomes, generating Ca²⁺ hotspots that boost phagocytosis. *Curr. Biol.* 22:1990–1997. <https://doi.org/10.1016/j.cub.2012.08.049>
- Orci, L., M. Ravazzola, M. Le Coadic, W.W. Shen, N. Demaurex, and P. Cosson. 2009. From the Cover: STIM1-induced precortical and cortical subdomains of the endoplasmic reticulum. *Proc. Natl. Acad. Sci. USA.* 106: 19358–19362. <https://doi.org/10.1073/pnas.0911280106>
- Papanikolaou, M., A. Lewis, and A.M. Butt. 2017. Store-operated calcium entry is essential for glial calcium signalling in CNS white matter. *Brain Struct. Funct.* 222:2993–3005. <https://doi.org/10.1007/s00429-017-1380-8>
- Perni, S., J.L. Dynes, A.V. Yeromin, M.D. Cahalan, and C. Franzini-Armstrong. 2015. Nanoscale patterning of STIM1 and Orail during store-operated Ca²⁺ entry. *Proc. Natl. Acad. Sci. USA.* 112:E5533–E5542. <https://doi.org/10.1073/pnas.1515606112>
- Picard, C., C.A. McCarl, A. Papolos, S. Khalil, K. Lüthy, C. Hivroz, F. LeDeist, F. Rieux-Laucat, G. Rechavi, A. Rao, et al. 2009. STIM1 mutation associated with a syndrome of immunodeficiency and autoimmunity. *N. Engl. J. Med.* 360:1971–1980. <https://doi.org/10.1056/NEJMoa0900082>
- Prakriya, M., and R.S. Lewis. 2002. Separation and characterization of currents through store-operated CRAC channels and Mg²⁺-inhibited cation (MIC) channels. *J. Gen. Physiol.* 119:487–507. <https://doi.org/10.1085/jgp.20028551>
- Prakriya, M., and R.S. Lewis. 2015. Store-Operated Calcium Channels. *Physiol. Rev.* 95:1383–1436. <https://doi.org/10.1152/physrev.00020.2014>
- Rungta, R.L., L.P. Bernier, L. Dissing-Olesen, C.J. Groten, J.M. LeDue, R. Ko, S. Drissler, and B.A. MacVicar. 2016. Ca²⁺ transients in astrocyte fine processes occur via Ca²⁺ influx in the adult mouse hippocampus. *Glia.* 64:2093–2103. <https://doi.org/10.1002/glia.23042>
- Samanta, K., P. Kar, G.R. Mirams, and A.B. Parekh. 2015. Ca(2+) Channel Relocalization to Plasma-Membrane Microdomains Strengthens Activation of Ca(2+)-Dependent Nuclear Gene Expression. *Cell Rep.* 12: 203–216. <https://doi.org/10.1016/j.celrep.2015.06.018>
- Schmidt, B., D. Alansary, I. Bogeski, B.A. Niemeyer, and H. Rieger. 2019. Reaction-diffusion model for STIM-ORAI interaction: The role of ROS and mutations. *J. Theor. Biol.* 470:64–75. <https://doi.org/10.1016/j.jtbi.2019.02.010>
- Schneider, C.A., W.S. Rasband, and K.W. Eliceiri. 2012. NIH Image to ImageJ: 25 years of image analysis. *Nat. Methods.* 9:671–675. <https://doi.org/10.1038/nmeth.2089>
- Scrimgeour, N., T. Litjens, L. Ma, G.J. Barritt, and G.Y. Rychkov. 2009. Properties of Orail mediated store-operated current depend on the expression levels of STIM1 and Orail proteins. *J. Physiol.* 587:2903–2918. <https://doi.org/10.1113/jphysiol.2009.170662>
- Sharma, P., and L. Ping. 2014. Calcium ion influx in microglial cells: physiological and therapeutic significance. *J. Neurosci. Res.* 92:409–423. <https://doi.org/10.1002/jnr.23344>
- Srikanth, S., B. Ribalet, and Y. Gwack. 2013. Regulation of CRAC channels by protein interactions and post-translational modification. *Channels (Austin).* 7:354–363. <https://doi.org/10.4161/chan.23801>
- Tinevez, J.Y., N. Perry, J. Schindelin, G.M. Hoopes, G.D. Reynolds, E. Laplantine, S.Y. Bednarek, S.L. Shorte, and K.W. Eliceiri. 2017. TrackMate: An open and extensible platform for single-particle tracking. *Methods.* 115:80–90. <https://doi.org/10.1016/j.ymeth.2016.09.016>
- Toth, A.B., A.K. Shum, and M. Prakriya. 2016. Regulation of neurogenesis by calcium signaling. *Cell Calcium.* 59:124–134. <https://doi.org/10.1016/j.ceca.2016.02.011>
- Toth, A.B., K. Hori, M.M. Novakovic, N.G. Bernstein, L. Lambot, and M. Prakriya. 2019. CRAC channels regulate astrocyte Ca²⁺ signaling and gliotransmitter release to modulate hippocampal GABAergic transmission. *Sci. Signal.* 12. eaaw5450. <https://doi.org/10.1126/scisignal.aaw5450>
- Tshuva, R.Y., E. Korkotian, and M. Segal. 2017. ORAI1-dependent synaptic plasticity in rat hippocampal neurons. *Neurobiol. Learn. Mem.* 140:1–10. <https://doi.org/10.1016/j.nlm.2016.12.024>
- Várnai, P., B. Tóth, D.J. Tóth, L. Hunyady, and T. Balla. 2007. Visualization and manipulation of plasma membrane-endoplasmic reticulum contact sites indicates the presence of additional molecular components within the STIM1-Orail Complex. *J. Biol. Chem.* 282:29678–29690. <https://doi.org/10.1074/jbc.M704339200>
- Walsh, C.M., M. Chvanov, L.P. Haynes, O.H. Petersen, A.V. Tepikin, and R.D. Burgoyne. 2009. Role of phosphoinositides in STIM1 dynamics and store-operated calcium entry. *Biochem. J.* 425:159–168. <https://doi.org/10.1042/BJ20090884>
- Yen, M., and R.S. Lewis. 2018. Physiological CRAC channel activation and pore properties require STIM1 binding to all six Orail subunits. *J. Gen. Physiol.* 150:1373–1385. <https://doi.org/10.1085/jgp.20171985>
- Yen, M., and R.S. Lewis. 2019. Numbers count: How STIM and Orail stoichiometry affect store-operated calcium entry. *Cell Calcium.* 79:35–43. <https://doi.org/10.1016/j.ceca.2019.02.002>
- Yen, M., L.A. Lokteva, and R.S. Lewis. 2016. Functional Analysis of Orail Concatemers Supports a Hexameric Stoichiometry for the CRAC Channel. *Biophys. J.* 111:1897–1907. <https://doi.org/10.1016/j.bpj.2016.09.020>
- Yeromin, A.V., J. Roos, K.A. Stauderman, and M.D. Cahalan. 2004. A store-operated calcium channel in *Drosophila* S2 cells. *J. Gen. Physiol.* 123: 167–182. <https://doi.org/10.1085/jgp.200308982>
- Zagotta, W.N., M.T. Gordon, E.N. Senning, M.A. Munari, and S.E. Gordon. 2016. Measuring distances between TRPV1 and the plasma membrane using a noncanonical amino acid and transition metal ion FRET. *J. Gen. Physiol.* 147:201–216. <https://doi.org/10.1085/jgp.201511531>
- Zhou, Y., X. Wang, X. Wang, N.A. Loktionova, X. Cai, R.M. Nwokonko, E. Vrana, Y. Wang, B.S. Rothberg, and D.L. Gill. 2015. STIM1 dimers undergo unimolecular coupling to activate Orail channels. *Nat. Commun.* 6:6395. <https://doi.org/10.1038/ncomms9395>
- Zweifach, A., and R.S. Lewis. 1995. Rapid inactivation of depletion-activated calcium current (ICRAC) due to local calcium feedback. *J. Gen. Physiol.* 105:209–226. <https://doi.org/10.1085/jgp.105.2.209>
- Zweifach, A., and R.S. Lewis. 1996. Calcium-dependent potentiation of store-operated calcium channels in T lymphocytes. *J. Gen. Physiol.* 107: 597–610. <https://doi.org/10.1085/jgp.107.5.597>

Supplemental material

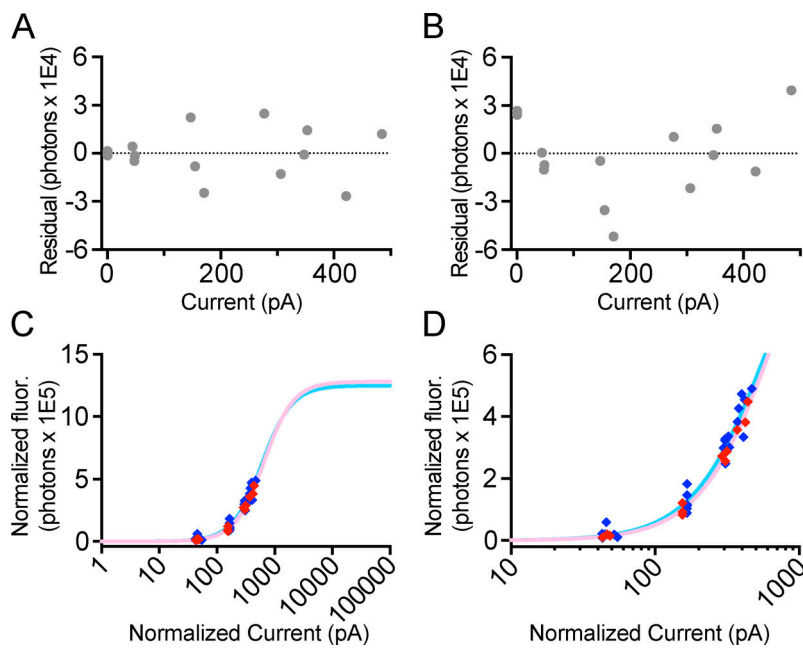


Figure S1. **Response function of Orai1-GCaMP6f.** (A and B) Residual plots for nonlinear curve fitting to the Hill equation (A; $R^2 = 0.992$) and linear regression (B; $R^2 = 0.978$) for the scatterplots of whole-cell current versus fluorescence shown in Fig. 4, C and D. (C and D) Scatterplots of normalized whole-cell current versus fluorescence for steps to increasingly negative membrane potentials (-10 , -40 , -70 , and -100 mV; cells A, E, and F; red diamonds) and for individual test pulses to negative membrane potentials (-10 , -40 , -70 , and -100 mV; cells A-F; blue diamonds). Lines indicate fitting to the Hill equation for a stepped test pulse (light red; $R^2 = 0.993$, $h_c = 1.7$ with 95% CI of 1.3–2.3) and for individual test pulses (light blue; $R^2 = 0.957$, $h_c = 1.7$ with 95% CI of 1.1–2.7). Note the high degree of overlap with similar maximum fluorescence values for the two fitted curves. (D) Enlargement of lower central portion of C. Whole-cell recordings were performed in 2 mM external Ca^{2+} .

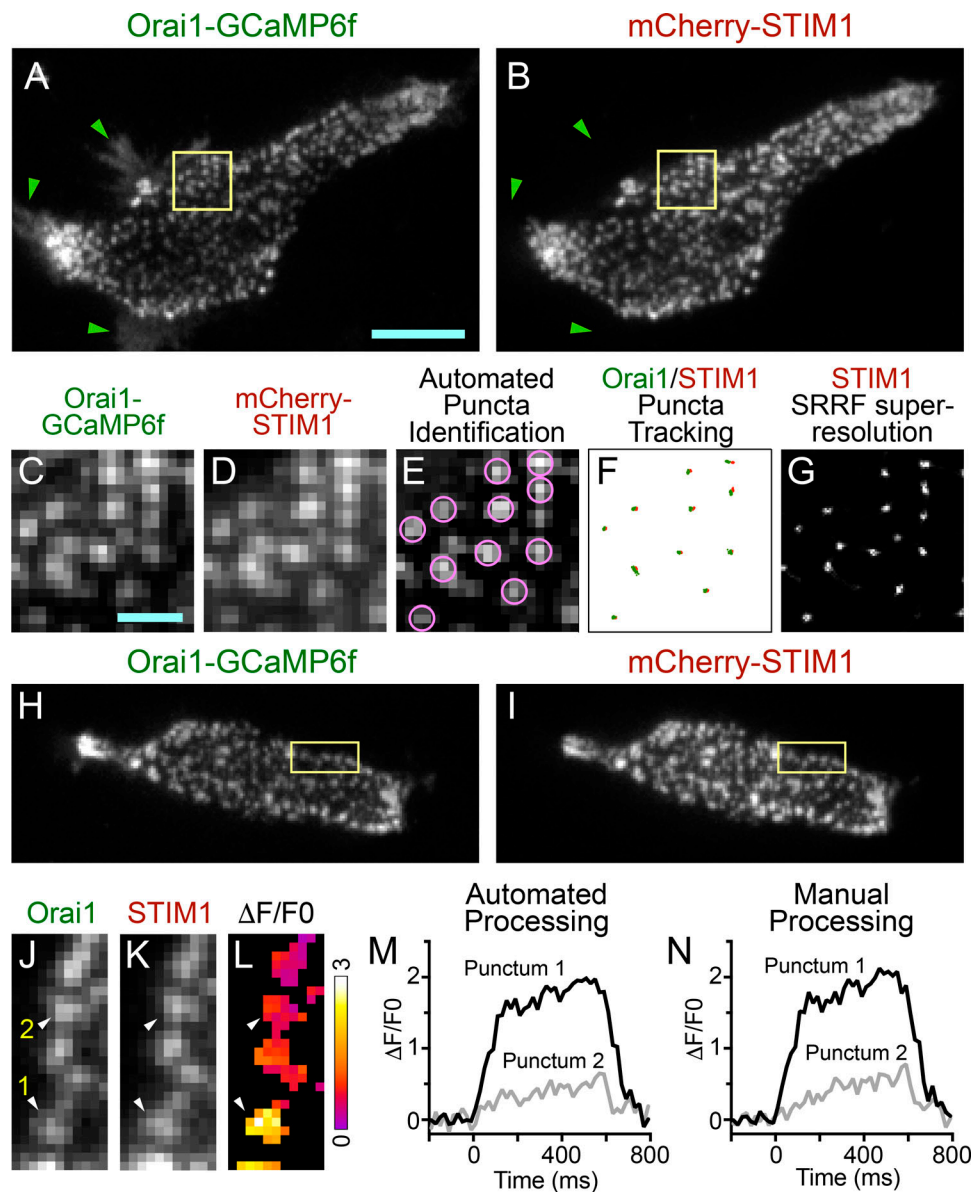


Figure S2. **Automated identification and recording from puncta.** (A and B) TIRF images of Orai1-GCaMP6f (A) and mCherry-STIM1 (B) from a transfected HEK 293A cell during whole-cell recording at +20 mV resting membrane potential (average of 10 frames). Green arrowheads indicate regions of diffuse Orai1-GCaMP6f fluorescence in corners and along edges of the TIRF footprint that lack STIM1-Orai1 puncta. (C and D) Cropped and enlarged portions of TIRF images corresponding to the yellow squares shown in A and B, respectively. (E) Puncta automatically identified by the program TrackMate, indicated by pink circles superimposed upon a local background-subtracted version of D. (F) Plot of puncta center for each of 50 consecutive frames for Orai1-GCaMP6f (green dots) and mCherry-STIM1 (red dots). Note that Orai1-GCaMP6f and mCherry-STIM1 positions are tightly clustered and clearly associated with the same punctum. (G) Corresponding SRRF computational superresolution image corresponding to D. (H and I) TIRF images of Orai1-GCaMP6f (H) and mCherry-STIM1 (I) from another transfected HEK 293A cell during whole-cell recording at +20 mV resting membrane potential (average of 10 frames). (J and K) Cropped, enlarged, and counterclockwise-rotated portions of TIRF images corresponding to the yellow rectangles shown in H and I, respectively. (L) Corresponding map of Orai1-GCaMP6f plateau $\Delta F/F_0$ for the region shown in J. Arrowheads in J–L indicate two puncta. (M and N) Corresponding graphs of $\Delta F/F_0$ for puncta 1 (black line) and puncta 2 (gray line) during a 600-ms test pulse to -100 mV measured using automated (M) and manually (N) positioned ROIs. Note the different magnitudes of $\Delta F/F_0$ for puncta 1 and 2. Scale bar in A is 10 μm (applies to B, H, and I), and the scale bar in C is 2 μm (applies to D–G and J–L). A–G correspond to cell C, and H–N correspond to cell D (see Fig. S3).

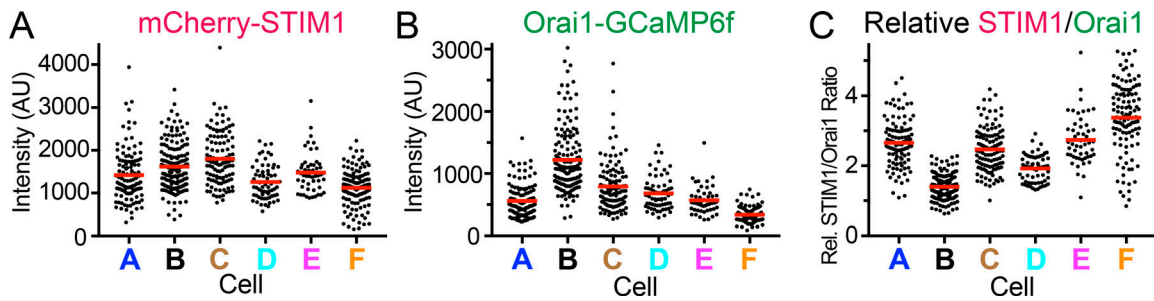


Figure S3. **mCherry-STIM1 and Orai1-GCaMP6f fluorescence at individual puncta.** (A and B) Fluorescence intensity of mCherry-STIM1 (A) and Orai1-GCaMP6f (B) at individual puncta from six different HEK 293A cells held at +20 mV holding potential. (C) Relative STIM1/Orai1 ratios for the same six cells. Red lines indicate the mean.

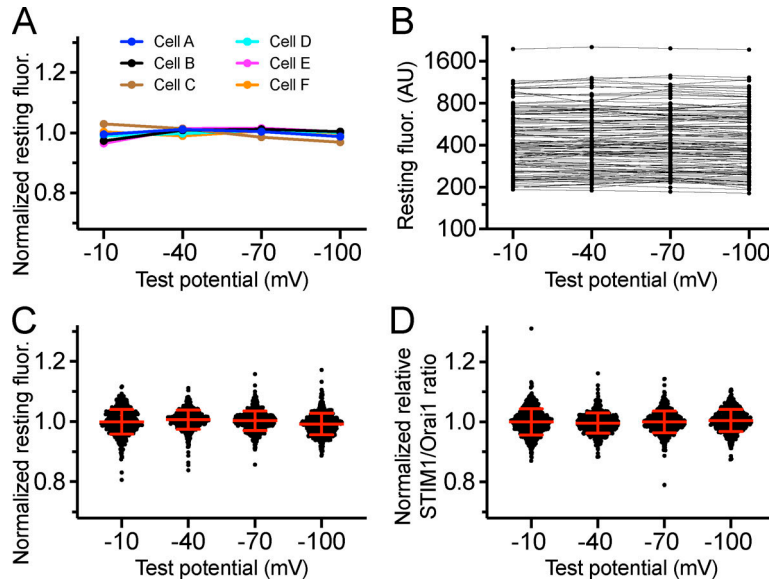
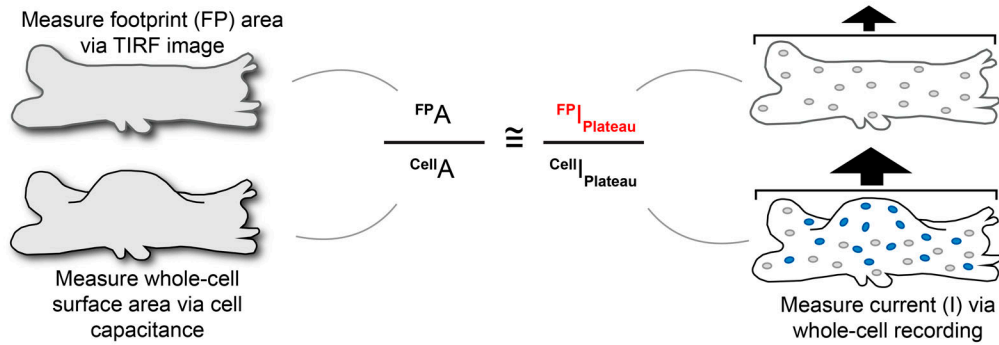
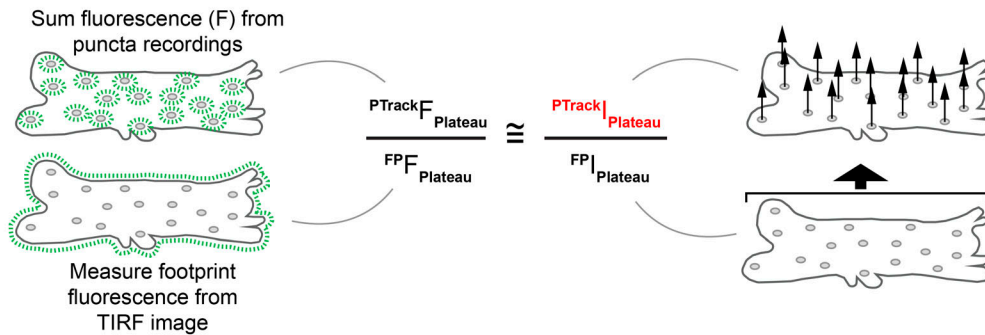


Figure S4. **Stability of Orai1-GCaMP6f resting fluorescence and relative STIM1/Orai1 ratio.** (A) Plots of Orai1-GCaMP6f resting fluorescence from each cell footprint, normalized to the average baseline value before four test pulses (-10, -40, -70, and -100 mV in 2 Ca). SD was 1.6% (24 total measurements). (B) Plots of Orai1-GCaMP6f resting fluorescence of 112 individual puncta from cell A (see Fig. S3). Note consistency in resting fluorescence for individual puncta. (C) Plots of normalized Orai1-GCaMP6f resting fluorescence from 535 individual puncta from cells A-F. (D) Plots of normalized relative STIM1/Orai1 ratio from 535 puncta from cells A-F. SDs of C and D were 3.6% and 3.8%, respectively (2,140 measurements each). Red lines in C and D are mean and SD. Relative STIM1/Orai1 ratio decreased by 0.7% between the first (-10 mV) and last (-100 mV) test pulses.

1. Use footprint area to calculate footprint current



2. Use fluorescence to calculate current through tracked puncta



3. Use [Ca²⁺] and resting fluorescence to calculate single puncta currents

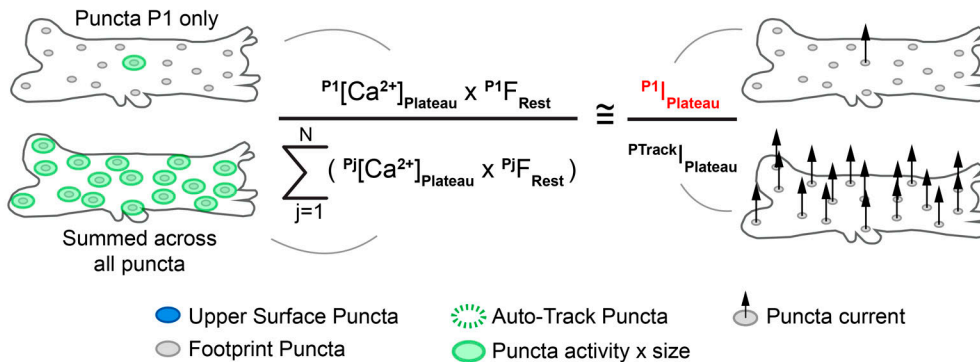


Figure S5. **Calculation of single puncta currents.** Superscripts refer to cell structures, such as the entire cell (Cell), footprint (FP), auto-tracked puncta (PTrack), or individual puncta (P1). Subscripts refer to cell fluorescence or current responses, such as resting (Rest) or Plateau. Results from each calculation are indicated in red.